arXiv:2205.02783v2 [cond-mat.mtrl-sci] 19 Aug 2022

Exciton–phonon interaction calls for a revision of the "exciton" concept

Fulvio Paleari[1,2] and Andrea Marini[1]

[1] *Istituto di Struttura della Materia and Division of Ultrafast Processes in Materials (FLASHit) of the National Research Council, via Salaria Km 29.3, I-00016 Monterotondo Stazione, Italy*
[2] *CNR-NANO, Via Campi 213a, 41125 Modena, Italy**

(Dated: August 22, 2022)

The concept of *optical exciton* — a photo–excited bound electron–hole pair within a crystal — is routinely used to interpret and model a wealth of excited–state phenomena in semiconductors. Beside originating sub–band gap signatures in optical spectra, *optical excitons* have also been predicted to condensate, diffuse, recombine, relax. However, all these phenomena are rooted on a theoretical definition of the excitonic state based on the following simple picture: "excitons" are actual particles that both appear as peaks in the linear absorption spectrum and also behave as well–defined quasiparticles. In this paper we show, instead, that the electron–phonon interaction decomposes the initial *optical* (i.e., "reducible") excitons into *elemental* (i.e., "irreducible") excitons, the latter being a different kind of bound electron–hole pairs lacking the effect caused by the induced, classical, electric field. This is demonstrated within a real–time, many–body perturbation theory approach starting from the interacting electronic Hamiltonian including both electron–phonon and electron–hole interactions. We then apply the results on two realistic and paradigmatic systems, monolayer MoS_2 (where the lowest–bound *optical exciton* is optically inactive) and monolayer $MoSe_2$ (where it is optically active), using first–principles methods to compute the exciton–phonon coupling matrix elements. Among the consequences of optical–elemental decomposition, we point to a homogeneous broadening of absorption peaks occurring even for the lowest–bound *optical exciton*, and we demonstrate this by computing exciton-phonon transition rates. More generally, our findings suggest that the *optical excitons* gradually lose their initial structure and evolve as *elemental excitons*. These states can be regarded as the real intrinsic excitations of the interacting system, the ones that survive when the external perturbation and the induced electric fields have vanished.

I. INTRODUCTION

The exciton concept is crucial to contemporary condensed matter physics and materials science, since it allows for a simple description of the response of the electrons in a crystal to an external electromagnetic field. In fact, the usual interpretation of spectroscopic experiments states that, when an electron–hole pair excitation is created in a (semiconducting) material, the Coulomb interaction will bind the pair creating an *exciton*[1].

Excitons and optical spectra. The excitonic picture stems from the interpretation of optical absorption spectra. Absorption is linked to the difference between the external field and the total field inside the material, including the contribution coming from the induced macroscopic polarization[2]. In fact, the exciton energies are just the frequencies of the time oscillation of the induced polarization[3], which in turn is determined by electronic charge oscillations induced by the external field. From a theoretical point of view, the excitonic picture is based on a combination of linear response theory — involving weak external fields — and many–body perturbation theory. In the usual treatment this leads to the well–known and widely used Bethe–Salpeter equation (BSE)[1,2]. The computational application of the BSE to a variety of realistic semiconducting systems has led to crucial advances in the field of theoretical optical spectroscopy[4,5]. In this paper, we will refer to excitations created by the interaction with an external electric field as *optical exciton* for the sake of clarity[6]. When an *optical exciton* appears inside the electronic band gap of a material, the exciton is said to be bound (the lowest-bound, optically active exciton thus defines the *optical* gap of the system). The strength of the binding depends on several factors but, in general, it is stronger in systems with wide optical gaps and low dimensionality due to weak screening of the electron–hole interaction[7]. Within linear response theory, excitonic properties are computed in practice via the Hamiltonian representation of the BSE[1]. When retardation effects[8] and electron–phonon interaction are neglected it is in fact possible to rewrite the excitonic state as an eigenstate of a pseudo–Hermitian matrix[5,9].

Excitons as real particles? Despite the fact that the pseudo–Hermitian structure of the BSE does not necessarily ensure that the exciton can be represented as a *real* bosonic particle[10], the possibility that these charge oscillations also correspond to real populations of nonequilibrium bound electron–hole pairs is highly debated. The question is how the interplay of the electromagnetic properties and internal structure of excitons may produce a real population and what is the role of the electron–phonon interaction in this process. In a real–particle picture, *optical excitons* are treated as bosons weakly coupled by an effective interaction. In the last few years several theoretical[11–13] and experimental[14–17] works have been using the real–particle assumption for *optical excitons*. The advent of ultra–fast physics has made it possible to investigate in real time the dynamics of photo–excited materials, increasing the interest in excitonic physics. Model calculations[18,19] have boosted the concept of excitons as real particles, providing intuitive

interpretations of the out–of–equilibrium experiments. Within this picture, *optical excitons* have been proposed to form, diffuse, relax, scatter and even condensate before recombining[12,13,20–25]. Also using linear–response inspired model Hamiltonians, excitonic features have been predicted to appear in time–resolved ARPES[13,15,26,27]. This approach has also been used to formulate an excitonic version of the semiconductor Bloch equation[28] with the aim of modelling exciton dynamics in transition metal dichalcogenides (TMDs)[12,13,29,30]. A relevant feature of this approach is that excitons are treated in the popular Wannier model[31–33], which describes excitons as a hydrogen–like energy level series stemming from parabolic electronic bands and having themselves a parabolic dispersion in reciprocal space. These studies cemented the very intuitive picture that after photo–excitation, the system can be described in terms of bound electron–hole pairs which are essentially the same as the ones observed in optical absorption.

The consensus on the *optical exciton* –as–particle picture is, however, not complete. In the paradigmatic case of MoS_2, for example, it was initially suggested that the observed rapid raise of the transient absorption signal was due to the ultra–fast formation of excitons[14], supported by model calculations based on the excitonic Bloch equations[19]. Smejkal and al.[34], however, interpreted the very same experimental results purely in terms of single–body charge migrations and using *ab initio* methods. Additionally, it has also been shown that a perfect bosonization of interacting electron–hole pairs is impossible due to their fermionic substructure retaining the usual indistinguishability and Pauli repulsion properties[35–37]. Finally, a natural consequence of treating *optical excitons* as real particles is that the lowest energy *optical exciton* must have an infinite lifetime (i.e., vanishing peak linewidth) since energy conservation does not allow any scattering. The same situation occurs in the electronic quasiparticle theory where the electronic linewidth is known to go to zero at the Fermi level.

The Exciton-Phonon coupling. The enormous interest in the excitonic dynamics has made it crucial to investigate the problem of exciton–phonon coupling. In this case, the main conceptual approach is again to consider excitons as bosons described by the BSE Hamiltonian. Indeed, motivated by the pioneering works of Toyozawa, Segall and Mahan[38–40], several authors have extended and upgraded the original model using many–body theory with the aim of performing fully first–principles simulations on realistic materials, focusing on exciton relaxation lifetimes[41], spectral functions[42] and exciton–phonon sidebands[43,44].

If the *optical exciton* is assumed to be a well–defined, boson–like particle, then the phonons can mediate the exciton–exciton interaction causing, for example, the dressing of the excitons and finite lifetimes[11,45]. This picture has been employed to describe phonon–assisted sidepeaks in absorption and luminescence spectra,[39,42,44,46–49] as well as the linewidths of exciton peaks[12,38,41,50]. The methodologies employed in the above references range from parametrised simple models to tight–binding treatments and fully first–principles descriptions.

Revisiting the exciton–phonon picture. Despite its success, the treatment of excitons as real particles remains an underinvestigated *assumption.* Thus, in this work we ask the following question: given that "excitons" and "phonons" are both excitations dressed by the same electron–electron interactions, is it always sound to treat them as "pristine" particles that may interact with each other? Or, rather, a proper account of their internal structures, consistent with the approximations we generally use to treat electronic interactions, may lead to a subtler picture? We aim to address this issue by considering the shaping of the exciton complex by both external light and lattice vibrations. To this end, we derive a theory describing the scattering of *optical excitons* with phonons. In deriving our theory we demonstrate that the *optical excitons* are scattered by the phonons in *"elemental" excitons*, undressed of the electron–hole exchange components, thus complicating the original simpler picture.[51] A graphical summary of this statement is presented in Fig. 1. A possible consequence is that *optical excitons*, as defined in photoabsorption, may not provide a suitable basis to describe excited–state dynamics and excitonic lifetimes, as well as to calculate phonon–assisted optical properties, especially in materials where electron–hole exchange interaction is large with respect to the excitonic binding energy. In order to explore this possibility, we perform fully first–principles exciton–phonon numerical simulations in monolayer MoS_2 and $MoSe_2$ with the goal of comparing the standard "real–particle" approach with the one proposed here. In particular, we show how *optical excitons* are decomposed in a packet including a large number of *elemental excitons* and how the homogeneous linewdith of even the lowest–bound *optical exciton* peak may be non–vanishing, according to our picture of exciton–phonon interaction. We provide a lower–bound estimate for these linewidths.

The paper is organised as follows. In Sec. II we introduce the many–body electronic Hamiltonian and the optical response function describing absorption, and in Sec. III we derive a generalised Bethe–Salpeter equation to account for "optical" or "elemental" excitonic properties. This is followed in Sec. IV by a discussion of the difference of the two pictures with *ab initio* results for monolayer MoS_2 and $MoSe_2$. The exciton–phonon coupling problem is introduced and worked out theoretically in Sec. V. Computational results for exciton–phonon coupling matrix elements and linewidths involving *optical* and *elemental* excitons in MoS_2 and $MoSe_2$ are reported in Sec. VI, which is followed by a discussion in Sec. VII. The main text is complemented by four Appendices, including one reporting the full computational details.

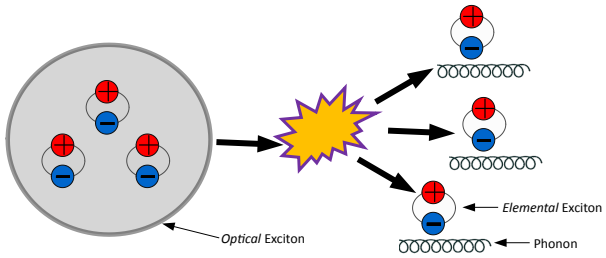


Figure 1. Simple exciton–phonon coupling sketch. The picture we propose in this work is that the optical excitation is decomposed into a distribution of *elemental excitons* – undressed of the Hartree interaction (i.e., the electron–hole exchange) — by electron–phonon interactions. This distribution is the real internal structure of the *optical exciton*. A remarkable consequence of this picture is that the lowest energy *optical exciton* has zero width in a real–particle representation, while if written in terms of *elemental excitons* acquires a finite, observable energy broadening.

II. EXTERNAL FIELDS AND THE EXCITON DEFINITION

The state–of–the art definition of *optical exciton* is based on the linear response of the interacting electron density to an external electromagnetic perturbation, which is described by the Bethe–Salpeter equation, used in standard first–principles calculation of optical absorption spectra[1,2,5]. As before, we will refer to this equation as *optical*–BSE, in order to keep it distinguished from the *elemental*–BSE describing the elemental excitons.

We follow the real–time approach of Refs.[52–54] in which our subsequent extension including dynamical electron–phonon interactions will also be formulated. Let us consider the Hamiltonian of the electronic system perturbed by a scalar external potential U_{ext}. We assume a purely longitudinal gauge with no external vector potentials.

$$\hat{H}(t) = \hat{H}_e + \int d\mathbf{r}\hat{\rho}(\mathbf{r}) U^{ext}(\mathbf{r},t), \tag{1a}$$

$$\hat{H}_e = \sum_i \hat{h}_i + \hat{W}_{e-e} + \hat{V}_{e-ion}. \tag{1b}$$

In Eq. (1a) $\hat{H}_e$ is the electronic Hamiltonian which includes the electron–electron ($\hat{W}_{e-e}$) and the *bare* electron–ion ($\hat{V}_{e-ion}$) interactions. U^{ext} represents the *total* time–dependent perturbation, which embodies the experimental field and the macroscopic part of the field induced in the material.

It is essential to note that, in Eq. (1), $\hat{V}_{e-ion}$ is not assumed to be screened from the beginning, as done in the previous works[41,42]. It has been, indeed, demonstrated[55] that such an assumption implies double–counting problems that can be avoided only by screening dynamically $\hat{V}_{e-ion}$ along with the solution of the BSE.

In Eq. (1) we have also introduced the electronic density operator $\hat{\rho}(\mathbf{r})$ and the single–particle Hamiltonian $\hat{h}_i$. Let us also mention the electron Green's function $G(\mathbf{r}_1t_1,\mathbf{r}_2t_2)$ associated with this Hamiltonian and recall that the density is given by $\rho(\mathbf{r}t) = \langle\hat{\rho}(\mathbf{r})\rangle = -\mathrm{i}G(\mathbf{r}t,\mathbf{r}^+t^+)$. By using diagrammatic methods the effect of $\hat{W}_{e-e}$ and $\hat{V}_{e-ion}$ is translated in a self–energy potential Σ which appears in the equation of motion for G, as we will discuss shortly. Σ is comprised of the classical Hartree interaction,

$$V^H(\mathbf{r},t) = \int' d\mathbf{r}'\rho(\mathbf{r}',t)\, v(\mathbf{r},\mathbf{r}'), \tag{2}$$

where $v(\mathbf{r},\mathbf{r}')$ is the bare Coulomb potential, plus an exchange and correlation part treatable at different levels of approximation[3]. The induced potential is actually the macroscopic average of V^H and we include it by definition in U^{ext}. Thus, the integral in Eq. (2) runs only on the spatial microscopic components. More details about this choice are provided in Appendix A.

The variation of the density with respect to the external field within linear order defines the electronic, optical response function χ_{opt}:

$$\chi_{opt}(\mathbf{r}_1t_1,\mathbf{r}_2t_2) = \left.\frac{\delta\rho(\mathbf{r}_1,t_1)}{\delta U^{ext}(\mathbf{r}_2,t_2)}\right|_{U^{ext}=0}. \tag{3}$$

Optical excitons are the poles of the Fourier transform of χ_{opt} with respect to the time difference. A key property of Eq. (3) is the appearance in the denominator of U^{ext}, which is a macroscopic field and the one that can be experimentally observed. This has a crucial impact on the definition of the *optical excitons*.

Let us now consider a hypothetical experimental apparatus able to also detect all the microscopic variations, induced by light absorption, of the *total* potential $U^{tot} = U^{ext} + V^H$. This corresponds to having an electric field detector with a spatial resolution tinier than the unit cell size of the system. As a consequence, in this case, the experimental observable would be described by a different response function, that we denote *elemental* and that is defined as:

$$\chi^{el}(\mathbf{r}_1t_1,\mathbf{r}_2t_2) = \left.\frac{\delta\rho(\mathbf{r}_1,t_1)}{\delta U^{tot}(\mathbf{r}_2,t_2)}\right|_{U^{ext}=0}. \tag{4}$$

Eq. (3) and Eq. (4) emphasize that the definition of *exciton* as an observable is determined by the measure process.

III. THE GENERALIZED BETHE–SALPETER EQUATION

Given the definitions Eq. (3) and Eq. (4) the corresponding *optical* and *elemental* BSEs can be easily derived by neglecting the electron–phonon interaction and using the non–local Hartree plus screened exchange (HSEX) scheme[1] in which Σ is written as the sum of the classical, mean–field Hartree term $\hat{V}_H$ with the statically

screened exchange interaction embodied in the "mass" term $\hat{M}_{SEX}$.

$$M^{SEX}\left(\mathbf{r}_1,\mathbf{r}_2,t\right)=\mathrm{i}G\left(\mathbf{r}_1t,\mathbf{r}_2t^+\right)W\left(\mathbf{r}_1,\mathbf{r}_2\right). \quad (5)$$

Here $W=\epsilon_H^{-1}v$ is the screened Coulomb interaction, and the static screening ϵ_H^{-1} is calculated in the Hartree (also called random phase, RPA) approximation[1].

In the following we will first introduce a convenient basis to write the Dyson equation. We will then derive from the Hedin's representation of the mass operator a generalized Bethe–Salpeter equation for the three–points electron–hole propagator. From this general equation we will derive the *optical*–BSE and *elemental*–BSE. Equipped with the two Bethe Salpeter equations, we resume our discussion of optical vs elemental excitons — leading to the problem of exciton–phonon coupling — in Section IV.

A. Dyson's equation in a generalized basis

The electronic Green's function (GF) $G\left(\mathbf{r}_1t_1,\mathbf{r}_2t_2\right)$ corresponding to the Hamiltonian Eq. (1) satisfies the Dyson equation for the single–particle Green's function[56]

$$G\left(\mathbf{r}_1t_1,\mathbf{r}_2t_2\right)=\int d\mathbf{r}_3\mathbf{r}_4dt_3t_4G^0\left(\mathbf{r}_1t_1,\mathbf{r}_3t_3\right)\left[\delta\left(t_2,t_3\right)\delta\left(\mathbf{r}_2,\mathbf{r}_3\right)+\Sigma\left(\mathbf{r}_3t_3,\mathbf{r}_4t_4\right)G\left(\mathbf{r}_4t_4,\mathbf{r}_2t_2\right)\right]. \quad (6)$$

The **exact** self–energy Σ corresponding to Eq. (1) has been derived, among others, in Ref. [57]:

$$\Sigma\left(\mathbf{r}_1t_1,\mathbf{r}_2t_2\right)=M\left(\mathbf{r}_1t_1,\mathbf{r}_2t_2\right)+ +V^H\left(\mathbf{r}_1,t_1\right)\delta\left(t_1,t_2^+\right)\delta\left(\mathbf{r}_1,\mathbf{r}_2\right), \quad (7)$$

with

$$M\left(\mathbf{r}_1t_1,\mathbf{r}_2t_2\right)=M^{e-e}\left(\mathbf{r}_1t_1,\mathbf{r}_2t_2\right)+M^{e-p}\left(\mathbf{r}_1t_1,\mathbf{r}_2t_2\right). \quad (8)$$

In Eq. (8) M^{e-e} and M^{e-p} are, respectively, the electron–electron (e-e) and the electron–phonon (e-p) terms. The approximated mass operator used in this work will be described later. We first want to derive some exact properties of the response function. We start by introducing a convenient single–particle representation:

$$G\left(\mathbf{r}_1t_1,\mathbf{r}_2t_2\right)=\sum_{ij}\overline{\phi}_i\left(\mathbf{r}_1\right)\phi_j\left(\mathbf{r}_2\right)G_{ij}\left(t_1,t_2\right), \quad (9)$$

with $\{\phi_i(\mathbf{r})\}$ a suitable complete basis (i represents a generic electronic band and $\mathbf{k}$–point). Thanks to Eq. (9) we can rewrite Eq. (6) in a compact form using a matrix notation

$$\underline{G}\left(t_1,t_2\right)=\underline{G}^0\left(t_1,t_3\right)\left[\delta\left(t_3,t_2\right)+\underline{\Sigma}\left(t_3,t_4\right)\underline{G}\left(t_4,t_2\right)\right]. \quad (10)$$

Quantities that depend on two electronic indices are represented as matrices $[\underline{O}]_{ij}$. In the following, more convoluted objects depending on four indices will appear. In this case we will represent them as tensors: $\left[\underline{\underline{O}}\right]_{\substack{ij\\kl}}$. The conventions used to represent tensorial operations are defined in Appendix B. The Einstein convention (assuming all repeated indices to be summed) is also implied.

B. The Generalized Bethe–Salpeter Equation

In the single–particle basis representation all response functions are tensors of rank 2. In particular we can define a generalized two–particle Green's function

$$L^{\eta}_{\substack{ij\\kl}}\left(t_1,t_2;t_3\right)\equiv\frac{\delta G_{ij}\left(t_1,t_2\right)}{\delta\eta_{kl}\left(t_3\right)}. \quad (11)$$

Eq. (11) is easily connected to the optical/elemental response functions. Indeed, by definition

$$\underline{\underline{\chi}}^{opt/el}\left(t_1,t_2\right)\equiv-i\,\underline{\underline{L}}^{\eta}\left(t_1,t_1^+;t_2\right)\big|_{\eta=U^{ext}/U^{tot}}. \quad (12)$$

Therefore in Eq. (11) η is an arbitrary field that, later, we will assume to correspond to U^{tot} or U^{ext} . We can work out Eq. (11) by differentiating Eq. (9)

$$\frac{\delta\underline{G}\left(t_1,t_2\right)}{\delta\underline{\eta}\left(t_3\right)}=\underline{G}^0\left(t_1,t_4\right)\left[\underline{\Sigma}\left(t_4,t_5\right)\underline{\underline{L}}^{\eta}\left(t_5,t_2;t_3\right)+ +\frac{\delta\underline{\Sigma}\left(t_4,t_5\right)}{\delta\underline{\eta}\left(t_3\right)}\underline{G}\left(t_5,t_2\right)\right]. \quad (13)$$

We now need to calculate $\frac{\delta\underline{\Sigma}(t_4,t_5)}{\delta\underline{\eta}(t_3)}$. By using the Dyson equation and the chain rule we get

$$\frac{\delta\underline{\Sigma}\left(t_4,t_5\right)}{\delta\underline{\eta}\left(t_3\right)}=\underline{G}^{-1}\left(t_4,t_6\right)\underline{\underline{L}}^{\eta}\left(t_6,t_7;t_3\right)\underline{G}^{-1}\left(t_7,t_5\right). \quad (14)$$

We see that the equation for L^{η} can be closed:

$$\underline{\underline{L}}^{\eta}(t_1,t_2;t_3) = \underline{G}(t_1,t_3)\,\underline{\underline{\delta}}\,\underline{G}(t_3,t_2) + \\ + \underline{G}(t_1,t_4)\left[\underline{\underline{\Xi}}(t_4,t_5;t_6,t_7) + \underline{\underline{K}}^{\eta}(t_4,t_6)\,\delta(t_4,t_5)\,\delta(t_6,t_7)\right]\underline{\underline{L}}^{\eta}(t_6,t_7;t_3)\,\underline{G}(t_5,t_2)\,. \quad (15)$$

In Eq. (15) we have introduced the tensorial delta function $\left[\underline{\underline{\delta}}\right]_{\substack{ij\\kl}} = \delta_{ik}\delta_{jl}$ and

$$\underline{\underline{\Xi}}(t_4,t_5;t_6,t_7) \equiv \frac{\delta \underline{\underline{M}}(t_4,t_5)}{\delta \underline{G}(t_6,t_7)}, \quad (16a)$$

$$\underline{\underline{K}}^{\eta}(t_4,t_6) \equiv \frac{\delta\left(\underline{U}^{tot}(t_4) - \underline{\eta}(t_4)\right)}{\delta \underline{G}(t_6,t_{6^+})}. \quad (16b)$$

Eq. (15) represents the *generalized BSE* and it allows to connect any self–energy Σ to the equation of motion for the two–particles green's function L.

C. The *optical* and *elemental* Bethe–Salpeter Equations

The *optical* (or reducible) BSE is obtained when $\eta(\mathbf{r},t) \equiv U^{ext}(\mathbf{r},t)$ and the electronic self–energy is approximated with the SEX expression neglecting electron–phonon effects. In this case

$$M^{e-e}_{ij}(t_1,t_2) \approx i\delta\left(t_2,t_1^+\right) \underset{kl}{W_{ij}} G_{kl}\left(t_1,t_1^+\right), \quad (17)$$

Where we defined

$$\underset{kl}{W_{ij}} \equiv \int d\mathbf{r}_1\mathbf{r}_2 \overline{\phi}_i(\mathbf{r}_1)\,\phi_k(\mathbf{r}_1)\,W(\mathbf{r}_1,\mathbf{r}_2)\,\overline{\phi}_l(\mathbf{r}_2)\,\phi_j(\mathbf{r}_2)\,. \quad (18)$$

It follows that

$$K^{opt}(t_4,t_6)_{\substack{ij\\kl}} = -iV^H_{\substack{ik\\jl}}\,\delta(t_4,t_6)\,, \quad (19a)$$

$$\Xi(t_4,t_5;t_6,t_7)_{\substack{ij\\kl}} = i\delta(t_1,t_2)\,\delta(t_4,t_{3^+})\,\underset{kl}{W_{ij}}. \quad (19b)$$

Here the repulsive term K^{opt} is determined by the microscopic components of the Hartree interaction, i.e., by the local field effects. This term is also known as electron–hole exchange because it swaps electron and hole indices with respect to Ξ, which is known instead as the direct or binding term. In this case Eq. (15) is closed in the space of two times, $\underline{\underline{L}}^{opt}(t_1,t_2) \equiv \underline{\underline{L}}\left(t_1,t_1^+;t_2\right)$, and

$$\underline{\underline{L}}^{opt}(t_1,t_2) = \underline{G}(t_1,t_2)\,\underline{\underline{\delta}}\,\underline{G}(t_2,t_1) + \\ + i\underline{G}(t_1,t_3)\left[\underline{\underline{W}} - \underline{\underline{V}}^H\right]\underline{\underline{L}}^{opt}(t_3,t_2)\,\underline{G}(t_3,t_1)\,. \quad (20)$$

The same procedure can be applied to derive the *elemental* (or irreducible) BSE which corresponds to taking $\eta(\mathbf{r},t) \equiv U^{tot}(\mathbf{r},t)$, from which follows $K^{el} = 0$. In this case, then, we have

$$\underline{\underline{L}}^{el}(t_1,t_2) = \underline{G}(t_1,t_2)\,\underline{\underline{\delta}}\,\underline{G}(t_2,t_1) + \\ + i\underline{G}(t_1,t_3)\,\underline{\underline{W}}\,\underline{\underline{L}}^{el}(t_3,t_2)\,\underline{G}(t_3,t_1)\,. \quad (21)$$

The last step we need is to connect the $L^{opt/el}$ to the diagonalization of the Bethe–Salpeter Hamiltonian, which is used in practice to compute exciton energies and wave functions. The procedure is outlined in Appendix C and leads to the definition of

$$\mathcal{H}^{opt}_{\substack{ij\\kl}} = \delta_{ik}\delta_{jl}\left(\epsilon_i - \epsilon_j\right) - \left(f_j - f_i\right)\left(\underset{kl}{W_{ij}} - \underset{kl}{K^{opt}_{ij}}\right). \quad (22)$$

Here again we see that, in the case of *optical excitons*, the repulsive term K^{opt} is given by the microscopic part of the total field inside the material. It is this purely electrostatic contribution which defines the *optical exciton*.

The two–particles Green's function relative to *elemental excitons* has the same form as above, but now only W appears in the definition of the excitonic Hamiltonian $\mathcal{H}^{el}$:

$$\mathcal{H}^{el}_{\substack{ij\\kl}} = \delta_{ik}\delta_{jl}\left(\epsilon_i - \epsilon_j\right) - \left(f_j - f_i\right)\underset{kl}{W_{ij}}. \quad (23)$$

It is essential to observe that both $\underline{\underline{W}}$ and $\underline{\underline{K}}^{opt}$ are, in general, pseudo–Hermitian matrices[9] and, therefore, even if their eigenvalues are real the left and right eigenvectors are different[10]. We assume here that $\mathcal{H}^{el/opt}$ are strictly Hermitian, so that once diagonalized we can finally write $\underline{\underline{L}}^{opt/el}$ in an excitonic representation. By calling $E^{opt/el}_{\lambda}$ the eigenvalues of $\underline{\underline{\mathcal{H}}}^{opt/el}$, we have that

$$L^{opt}(\omega) = \sum_{\lambda} \frac{1}{\omega + i0^+ - E^{opt}_{\lambda}}, \quad (24a)$$

$$L^{el}(\omega) = \sum_{\lambda} \frac{1}{\omega + i0^+ - E^{el}_{\lambda}}. \quad (24b)$$

The picture that follows from the Hamiltonian representation of the BSE is simple: an *optical/elemental* exciton is a superposition of electron–hole pairs weighted by the eigenvectors of the excitonic Hamiltonian, whose components we call $\underline{A}^{opt/el}_{\lambda}$:

$$|\lambda^{opt/el}\rangle = \sum_{ij} A^{ij,opt/el}_{\lambda} |i\rangle \otimes |j\rangle. \quad (25)$$

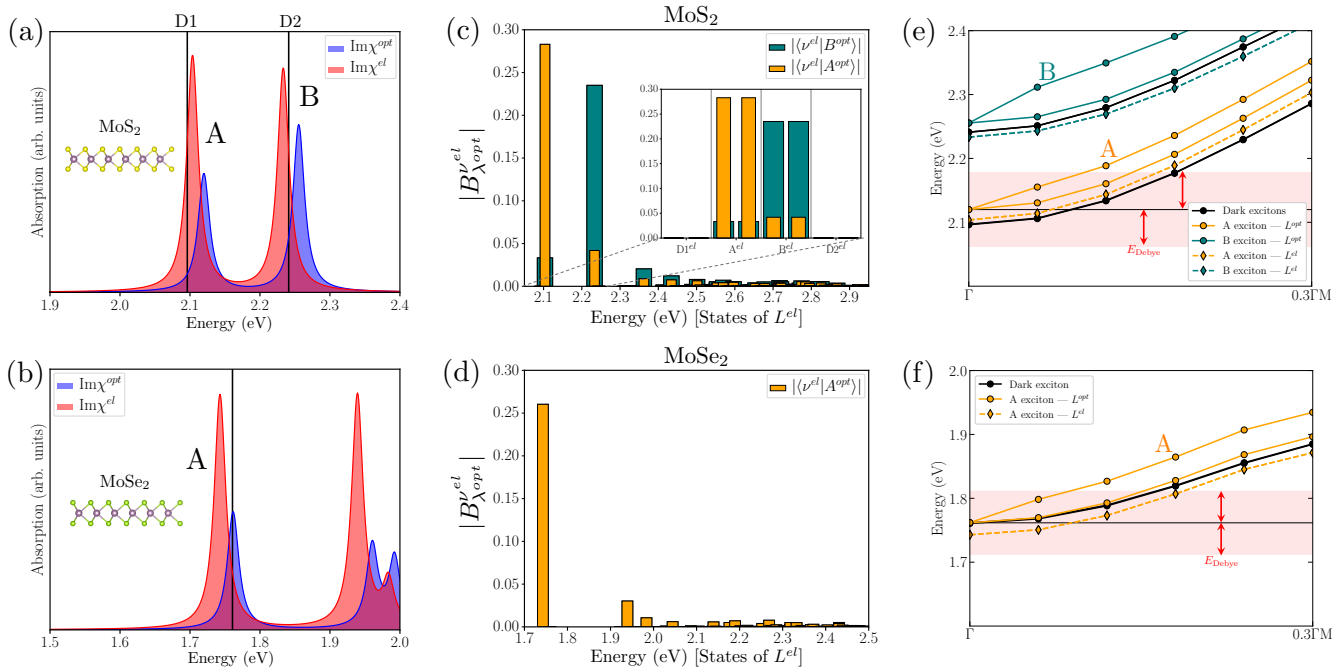


Figure 2. *Optical* and *elemental* excitons compared in the case of monolayer MoS_2 (upper panels) and monolayer $MoSe_2$ (lower panels). Panels (a–b): *Optical* (blue) and *elemental* (red) spectrum. The black vertical lines represent the dark states, while the peak "A" and "B" labels represent the established names for the relative bright peaks in the literature. In the insets showing the lattice geometry the gray balls represent Mo atoms, the yellow (green) ones represent S (Se) atoms. A set broadening parameter of 10 meV was used for the peaks. Panels (c–d): Projections (normalised) of A and B *optical excitons* onto the *elemental excitons* (see Eq. (27)). The projections of the A (B) optical excitons are shown in orange (teal). The inset shows a zoom around the low–lying dark (D1, D2) and bright (A, B) states of MoS_2 (they are all doubly degenerate). Panels (e–f): Exciton dispersion curves. Full lines and circles: *optical* excitons (including K^{opt}–driven degeneracy splittings). Dashed lines and diamonds: *elemental* excitons. The orange (teal) lines track the dispersion of the A (B) excitons. Black lines follow the dispersion of the dark states. The red shaded regions marks the energy–allowed region for the exciton–phonon scattering of the A exciton at Γ (one Debye energy).

IV. ABSORPTION SPECTRA: *OPTICAL* AND *ELEMENTAL* EXCITONS

The differences between *optical excitons* and *elemental excitons* states are analyzed in detail in Fig. 2 for two paradigmatic TMDs: monolayer MoS_2 (upper panels) and monolayer $MoSe_2$ (lower panels). Naturally, the strength and role of the matrix elements of K^{opt} are of particular interest to us. Since this is a repulsive contribution, lowering the binding energy of the excitons, χ^{el} may have in general more tightly bound excitons than χ^{opt}. Furthermore, the strength of the excitonic coupling with light is also affected, since it depends on the exciton wave functions.

Optical absorption is connected to the imaginary part of the macroscopic dielectric function ϵ_M, which is given by the $q \to 0$ limit of the response function χ[2,5]:

$$\mathrm{Im}\epsilon_M^{\eta}(\omega) \propto \mathrm{Im}\lim_{q\to 0}\chi^{\eta}(q,\omega) = \sum_{\lambda} |\sum_{ij} A_{\lambda}^{ij,\eta} d_{ij}|^2 \delta(\omega - E_{\lambda}^{\eta}). \tag{26}$$

Here, d_{ij} is the optical matrix element for the light–induced electronic transition between states i and j, calculated in the dipole approximation.

In Fig. 2a–b the absorption spectra of the two kinds of excitons are shown. The red region corresponds to the absorption from *elemental excitons*, while the blue region from *optical excitons*. Each bright exciton also has a dark companion, shown with a black vertical line, in which $K^{opt} = 0$ always because of the opposite spin polarisation of electron and hole.[58–60] Thus, dark states always coincide in both the optical and the elemental cases. Conversely, the energy of the bright states changes and shifts downwards. In particular, the B exciton in MoS_2 and the A exciton in $MoSe_2$ both slide below the energy of their dark companions. The latter case is notable because it means that in $MoSe_2$ the lowest *optical*–BSE state is dark, whereas the lowest *elemental*–BSE is bright. The energy difference between the corresponding optical and elemental states are: $\Delta^{MoS_2}A = 16$ meV, $\Delta^{MoS_2}B = 22$ meV and $\Delta^{MoSe_2}A = 19$ meV. Their intensity also noticeably changes, with K^{opt} accounting for a large increase of the B exciton with respect to the A one in MoS_2, while in the *elemental* case they have almost the same intensity.[61]

The relationship between optical and elemental excitons can be further elucidated by looking at the decomposition of one type into the other, defining the projections

$$B^{\nu^{el}}_{\lambda^{opt}} = \sum_{ij} \overline{A^{ij,el}_{\nu}} A^{ij,opt}_{\lambda} = \left\langle \nu^{el} \right| \left. \lambda^{opt} \right\rangle . \qquad (27)$$

In Fig. 2c–d we report the calculated projections (values of $|B^{\nu^{el}}_{\lambda^{opt}}|$) of the lowest–bound *optical excitons* onto the *elemental excitons* of MoS_2 (c) and $MoSe_2$ (d). In the case of MoS_2 there are two bound states (A and B) while in $MoSe_2$ only A. Let us first look at the inset in Fig. Fig. 2(c); here we see that despite the A and B excitons of MoS_2 being formed by different eletronic transitions (the difference is due to spin–orbit coupling), they both partially decompose onto each other: the A *optical exciton* has a sizable component onto the B *elemental exciton* and viceversa. This was already noted in Ref. 61: however, the decomposition shown in the inset only accounts for 30% of the projection components, as can be evinced by looking at the complete figure which includes up to 450 *elemental* excitonic states. A large number of exchange–less excitonic states, much higher in energy than the A and B ones, have nonzero projections with the optical A and B states, accounting for the remaining 70% of the strength. This suggests that a large distribution of (elemental) states may play a role in the processes of optical–elemental scatterings and exciton dynamics. The same is true in the case of the A exciton in $MoSe_2$.

In Fig. 2e–f we report the exciton dispersions obtained by solving the *optical*–BSE (full lines) and *elemental*–BSE (dashed lines) at finite momenta. These states, not observable with optical light[16], correspond to electronic transitions in which the electron momentum k and the hole momentum k' differ as $k - k' = q$. The plots are made close to $q = 0$ (Γ) and along the direction ΓM in the hexagonal, two–dimensional BZ of these systems. We see that the bright A (orange color) and B (teal color) excitons, as well as their dark companions (black color), are doubly degenerate states. In particular, in addition to the energy shifts between optical and elemental bright excitons, we see that the presence of the Hartree contribution in the *optical* case causes a splitting of the bright excitons at finite momentum, something that is completely absent in the *elemental* case. Moreover, K^{opt} causes the higher energy split state to have a linear behavior with respect to $|q|$ — something that is well–known in the literature[58,62] — instead of the parabolic dispersion typical of W, which appears for all other states. If we consider for example the A excitons at Γ, we know that the scattering to finite–q states mediated by one phonon can take place in an energy window with the size of the Debye energy (59 meV in MoS_2, 50 meV in $MoSe_2$ according to our *ab initio* calculation). This window is shown by the red shaded region: we can clearly see how, depending on the kinds of initial and final excitonic states to be considered in our exciton–phonon description, the scattering dynamics may be quite different. This is particularly relevant because the intraband, low–q scattering mediated by acoustic phonons is predicted to account for a large part of the excitonic homogeneous linewidths.[63,64]

V. THE EXCITON–PHONON SCATTERING

Several different theoretical approaches to the derivation of exciton–phonon coupling for computational purposes are available in the literature.[41,42,44] All current approaches share the conceptual basis of the pioneering modellistic works of Toyozawa[38,40] and Segall, Rudin and Mahan[39,46]. This theory is based on three core assumptions: *optical excitons* and *elemental excitons* are the same, the excitonic Hamiltonian representation is taken as granted and the electron–phonon interaction appearing in the Hamiltonian is screened from the beginning.

By assuming that only one kind of excitons η exists, this theory also assumes $\mathcal{H}^{\eta}$ to be a physical Hamiltonian. The eigenvectors of $\mathcal{H}^{\eta}$ are then used to define excitonic creation and annihilation operators $\left[\hat{B}^{\eta}_{\lambda}\right]^{\dagger}$ and $\hat{B}^{\eta}_{\lambda}$, while $\mathcal{H}^{\eta}$ is rewritten as

$$\hat{\mathcal{H}}^{\eta} \approx \sum_{\alpha q} E^{\eta}_{\alpha q} \left[\hat{B}^{\eta}_{\alpha q}\right]^{\dagger} \hat{B}^{\eta}_{\alpha q}. \qquad (28)$$

An additional, crucial — and strong[35–37] — assumption in Eq. (28) is that excitons are good bosons in the sense that they satisfy bosonic commutation relations.

Now, by analogy with the electronic case, this bosonised treatment introduces exciton–phonon interaction into Eq. (28) in the form

$$\hat{\mathcal{H}}^{\eta}_{e-p} = \sum_{\alpha\alpha'\mu q q'} \mathcal{G}^{\mu q'}_{\alpha\alpha' q} \left(\hat{b}_{\mu q'} + \hat{b}^{\dagger}_{\mu -q'}\right) \left(\hat{B}^{\eta}_{\alpha' q+q'}\right)^{\dagger} \hat{B}^{\eta}_{\alpha q}. \qquad (29)$$

This term represents the η–exciton–phonon interaction with $\hat{b}_{\mu}$ being the phonon destruction operator for the phonon of branch μ and momentum q'. The crucial quantity in Eq. (29) is the exciton–phonon coupling matrix element $\mathcal{G}^{\mu q'}_{\alpha\alpha' q}$.

Clearly Eq. (29) makes sense only if it is possible to demonstrate that the case $\eta = opt$ involves only *optical excitons*. We will demonstrate in the next section that this is, actually, not possible. Moreover a crucial consequence of Eq. (29) is that the Fermi golden–rule predicts the excitonic linewidths, $\gamma_{\alpha q}$, of the state α with momentum $\mathbf{q}$ to have the form

$$\gamma_{\alpha q} \propto \sum_{\mu\beta q'} |\mathcal{G}^{\mu q'}_{\alpha\beta q}|^2 \delta(E^{opt}_{\alpha q} - E^{opt}_{\beta q+q'} \pm \Omega_{\mu q'}). \qquad (30)$$

Eq. (30) has been used, for example, in Refs. [41 and 42] and predicts the lowest *optical exciton* to have zero width.

Below, we will outline a derivation of the exciton–phonon coupling starting from the electronic Hamiltonian, Eq. (1), with electron–phonon interactions explicitly included from the start. This will allow us to overcome several of the assumptions underpinning the "bosonised" excitons model.

A. The vertex function

The *exact*[57] electron–phonon self–energy is:

$$M^{e-p}_{ij}(t_1,t_2) = i\sum_{\mu} G_{lm}(t_1,t_3)\times \\ \times\left(\underline{\underline{\Gamma}}^{el}(t_3,t_2;t_4)\,\underline{\underline{D}}^{\mu}(t_4,t_1)\right)_{\substack{mj\\ il}}. \quad (31)$$

Eq. (31) is written in the reference single particle basis defined in Eq. (9), G is the single–particle GF, while D is the *dressed* phonon propagator and Γ^{el} is the *elemental*/irreducible vertex function, given by:

$$D^{\mu}_{\substack{ij\\ kl}}(t_1,t_2) = g^{\mu}_{ik}(t_1)\,D^{\mu}(t_1,t_2)\,g^{\mu}_{lj}(t_2), \quad (32a)$$

$$\Gamma^{el}_{\substack{mj\\ np}}(t_3,t_2;t_4) = -\frac{\delta G_{mj}(t_3,t_2)}{\delta U^{tot}_{np}(t_4)}. \quad (32b)$$

In Eq. (32a) $g^{\mu}(\mathbf{r},t)$ is the *dressed* and time–dependent electron–phonon interaction along the phonon normal mode direction μ. Here we calculate it with state–of–the–art first–principles Density Functional Perturbation Theory (DFPT), where the matrix elements are given by[65]

$$g^{\mu}_{ij}(t) \approx g^{\mu}_{ij} = \frac{1}{\sqrt{2\Omega_{\mu}}}\int \mathrm{d}^3\mathbf{r}_1\mathbf{r}_2\overline{\phi_i(\mathbf{r}_1)}\times \\ \times\,\varepsilon^{-1}_{Hxc}(\mathbf{r}_1,\mathbf{r}_2)\partial_{\mu}\big|_{eq}V_{e-ion}(\mathbf{r}_2)\phi_j(\mathbf{r}_1). \quad (33)$$

In this expression, $\Omega_{\mu q}$ are the "adiabatic" phonon frequencies that may be computed in DFPT and are already renormalised by the static $V_H + V_{xc}$ interaction, $\{\phi_i(\mathbf{r})\}$ are the Kohn–Sham eigenfunctions of the DFT electronic problem, and finally ε^{-1}_{Hxc} is the static dielectric function again describing the screening of lattice vibrations by the interacting electronic system. In Fig. 3 the dressed $\underline{g}$ is represented by the filled box (■).

The GF appearing in Eq. (32) is the exact one, solution of Eq. (9) with self–energy including M^{e-p}. This is a self–consistent problem requiring a resummation to all orders the e–e and e–p interactions. Here we are interested, however, in the lowest order exciton–phonon scattering. This is consistent with *ab initio* approaches based on the Debye–Waller plus Fan–Migdal approximations[65].

In the present context we can linearize Eq. (32b) by approximating the $\underline{G}$ appearing on the r.h.s. with the electronic one, solution of the Dyson equation within the SEX approximation. This is a crucial approximation as it corresponds exactly to the excitonic vertex:

$$\Gamma^{el}_{\substack{ij\\ kl}}(t_3,t_4) \equiv \frac{\delta M^{SEX}_{ij}(t_3)}{\delta U^{tot}_{kl}(t_4)}. \quad (34)$$

A key step now is to rewrite Γ^{el} in terms of the excitonic propagator. Indeed by using Eqs. (17) and (11) we get

$$\Gamma^{el}_{\substack{ij\\ kl}}(t_1,t_2) = \delta_{ik}\delta_{jl} + iW_{\substack{ik\\ mn}}L^{el}_{\substack{mn\\ kl}}(t_1,t_2). \quad (35)$$

Thanks to Eq. (35) the e–p mass operator can be finally rewritten in terms of L^{el}:

$$M^{e-p}_{ij}(t_1,t_2) = i\sum_{\mu} G_{lm}(t_1,t_3)\left[\left(\underline{\underline{\delta}}\delta(t_2-t_4) + \right.\right. \\ \left.\left. +\underline{\underline{W}}\,\underline{\underline{L}}^{el}(t_2,t_4)\right)\underline{\underline{D}}^{\mu}(t_4,t_1)\right]_{\substack{mj\\ il}}, \quad (36)$$

Eq. (31) and Eq. (35) are essential ingredients of our theory and require further discussion. The diagrammatic form of Eq. (31) is shown in Fig. 3. It is already clear that the appearance of L^{el}, via Eq. (35), in M^{e-p}, will play a crucial role in the following of the theory. The question is, then, if it were possible to define M^{e-p} in terms of L^{opt}. The answer is no and the reason is that the $\hat{V}_{e-ion}$ potential appearing in Eq. (1) is bare, by definition. The phonon propagator calculated within state–of–the–art, first–principles DFPT is defined in terms of the *screened* variation of the ionic potential, as seen before. The inverse dielectric function appearing in Eq. (33) is, in DFPT, approximated with the static DFT inverse response functions. As discussed in Ref. 55 the dressing of V_{e-ion} absorbs the exchange scatterings from the vertex function and this is the reason why in Eq. (31) the elemental vertex appears.

B. The exciton–phonon kernel

Equation (35) connects the e–p mass operator to the *elemental* excitonic GF. This is a key property that permits to calculate correctly the exciton–phonon interaction. The next step now is to link M^{e-p} to the *optical*–BSE and its associated response function. To this end we go back to the two–times electron–hole GF,

$$L^{opt}_{\substack{ij\\ kl}}(t_1,t_2) \equiv \frac{\delta G_{ij}\left(t_1,t_1^{+}\right)}{\delta U^{ext}_{kl}(t_2)}, \quad (37)$$

and to its corresponding response function $\underline{\underline{\chi}}^{opt}(t_1,t_2) \equiv -i\underline{\underline{L}}^{opt}(t_1,t_2)$. The equation of motion for L^{opt} can be derived with the Schwinger approach, i.e., by using the functional derivatives to manipulate Eq. (37), exactly as we did for the time–dependent generalized BSE in Sec.III.[53]

This procedure, along with the help of Eq. (36) and Eq. (16a), leads to the e–p contribution to the generalized

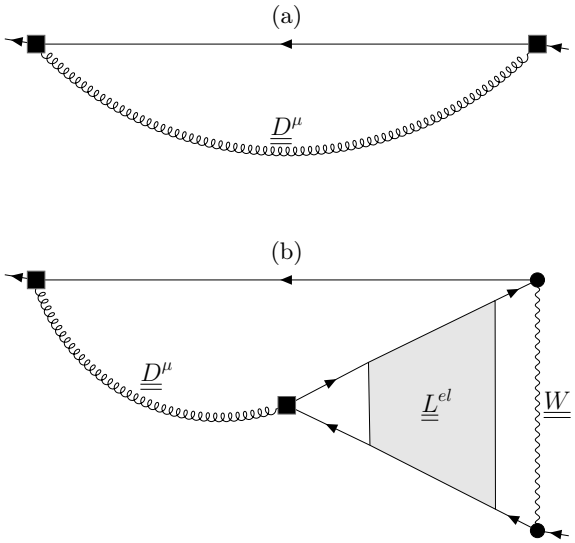


Figure 3. Diagrammatic decomposition of the M^{e-p} mass operator in terms of elemental electron–hole Green's function. (a) The well–known Fan–Migdal self–energy (M^{e-p} reduces to this when $\underline{\underline{\Gamma}}^{el} = \underline{\underline{\delta}}$). The straight (curly) line represents the electronic (phononic) GF and the filled box (■) is the dressed e-p coupling matrix element $\underline{g}$ from Eq. (33). (b) Vertex part of the self–energy from Eq. (36): this is the driving mechanism of the exciton–phonon coupling as explained the text. The vertex function is written in terms of the elemental/irreducible excitonic propagator $\underline{\underline{L}}^{el}$ and the statically screened electronic interaction $\underline{\underline{W}}$ (wiggly line).

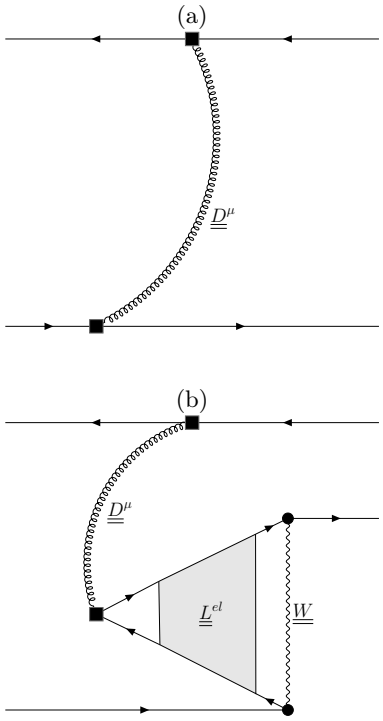


Figure 4. The two terms contributing to $\Xi^{e-p}\big|_G$, Eq. (40). Note that diagram (b) represents a renormalization of the electron–phonon vertex.

BSE kernel. Indeed we have that

$$\underline{\underline{\Xi}}\left(t_4,t_5;t_6,t_7\right) = \underline{\underline{\Xi}}^{e-e}\left(t_4,t_5;t_6,t_7\right) + \underline{\underline{\Xi}}^{e-p}\left(t_4,t_5;t_6,t_7\right), \quad \text{(38a)}$$

and,

$$\underline{\underline{\Xi}}^{e-e}\left(t_4,t_5;t_6,t_7\right) = i\delta\left(t_1,t_2\right)\delta\left(t_4,t_{3^+}\right)\underline{\underline{W}}, \quad \text{(38b)}$$

the last line being the same as that of Eq. (19) already obtained in the previous Section. $\underline{\underline{\Xi}}^{e-p}$ can then be also obtained by functionally deriving Eq. (36) with respect to $\underline{G}$. We see that $\underline{\underline{M}}^{e-p}$ depends on G via G_{lm}, $\underline{\underline{W}}$, $\underline{\underline{L}}^{el}$ and $\underline{\underline{D}}$.

We now adopt the usual approximation used to derive the *optical*–BSE where $\frac{\delta \underline{\underline{W}}}{\delta \underline{G}}$ is neglected. In addition we assume that the phonon propagator is calculated with DFPT, which implies that also $\frac{\delta \underline{\underline{D}}}{\delta \underline{G}} = 0$. Those approximations do not alter the main finding of this section.[66]

We are left, therefore, with two terms

$$\underline{\underline{\Xi}}^{e-p}\left(t_4,t_5;t_6,t_7\right) = \underline{\underline{\Xi}}^{e-p}\left(t_4,t_5;t_6,t_7\right)\big|_G + \underline{\underline{\Xi}}^{e-p}\left(t_4,t_5;t_6,t_7\right)\big|_L . \quad \text{(39)}$$

The first term of Eq. (39) is easy to evaluate

$$\left.\Xi^{e-p}{}_{\substack{ij\\kl}}\left(t_1,t_2;t_5,t_6\right)\right|_G = i\sum_{\mu}\left[\left(\underline{\underline{\delta}}\delta\left(t_2-t_4\right) + \underline{\underline{W}}\,\underline{\underline{L}}^{el}\left(t_2,t_4\right)\right)\underline{\underline{D}}^{\mu}\left(t_4,t_1\right)\right]_{\substack{lj\\ik}}, \quad \text{(40)}$$

and is graphically represented in Fig. 4. From the diagrammatic representation we see that $\Xi^{e-p}|_G$, physically, corresponds to a free electron–hole pair exchanging a phonon lines. It is, in practice, a phonon–mediated electron–hole scattering term. This scattering occurs at the level of free electron–hole pairs via a DFPT e–p interaction potential, Fig. 4(a), and with a renormalized interaction caused by the exciton–level electron–hole scatterings embodied in $\underline{\underline{L}}^{el}$, Fig. 4(b).

The second term of Eq. (40) to be calculated is $\Xi^{e-p}|_L$. This corresponds to the functional derivative of $\underline{\underline{L}}^{el}$ with respect to G. In order to proceed we observe that, by definition,

$$\frac{\delta \underline{\underline{L}}^{el}\left(t_2,t_4\right)}{\delta \underline{G}\left(t_5,t_6\right)} = \underline{\underline{L}}^{el}\left(t_2,t_7\right)\frac{\delta\left[\underline{\underline{L}}^{el}\left(t_7,t_8\right)\right]^{-1}}{\delta \underline{G}\left(t_5,t_6\right)}\underline{\underline{L}}^{el}\left(t_8,t_4\right). \quad \text{(41)}$$

In order to calculate $\frac{\delta[L]^{-1}}{\delta G}$ we notice that from the equation of motion for L^{el}, Eq. (21), it follows that

$$\left[\underline{\underline{L}}^{el}(t_7,t_8)\right]^{-1} = \left(\underline{G}(t_8,t_7)\,\underline{\delta G}(t_7,t_8)\right)^{-1} - i\underline{\underline{W}}. \quad (42)$$

Hence, it also follows that

$$\frac{\delta \underline{\underline{L}}^{el}(t_2,t_4)}{\delta \underline{G}(t_5,t_6)} = \underline{\underline{L}}^{el}(t_2,t_7)\left[\underline{\underline{L}}^{0}(t_7,t_6)\right]^{-1}\left[\underline{\delta}\,\underline{G}(t_6,t_5) + \underline{G}(t_6,t_5)\,\underline{\delta}\right]\left[\underline{\underline{L}}^{0}(t_5,t_8)\right]^{-1}\underline{\underline{L}}^{el}(t_8,t_4). \quad (43)$$

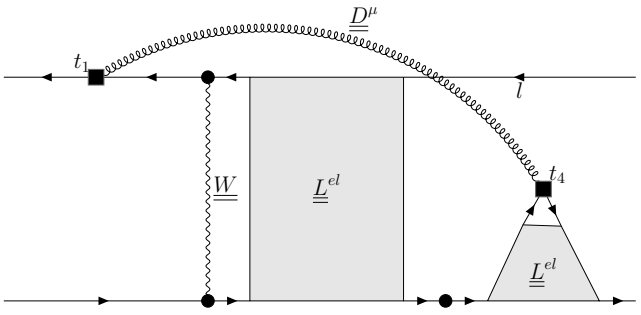


Figure 5. Graphical representation of the most important diagram contributing to the exciton–phonon kernel. This arises from the change in the *elemental exciton* GF and it splits L^{el} in two terms. One re-creates the internal exciton (four point function) while the other dresses the e–p interaction.

Equation (43) may appear complicated but it actually encodes in mathematical form a simple diagrammatic procedure. Indeed the convolution of $\underline{\underline{L}}^{el}$ with $\left[\underline{\underline{L}}^{0}\right]^{-1}$ corresponds to the action of removing the last free electron–hole pair propagator from the series of diagrams that build $\underline{\underline{L}}^{el}$. In this way we get the final form of $\Xi^{e-p}|_L$:

$$\left.\Xi^{e-p}_{\substack{ij\\kl}}(t_1,t_2;t_5,t_6)\right|_L = \\ = iG_{nm}(t_1,t_2)\left[W_{\substack{mj\\pq}}\frac{\delta L^{el}_{\substack{pq\\rs}}(t_2,t_4)}{\delta G_{kl}(t_5,t_6)}D^{\mu}_{\substack{rs\\in}}(t_4,t_1)\right]. \quad (44)$$

Eq. (44) leads to two contributions. The first is represented in Fig. 5 while the second corresponds to the dressed electron–phonon scattering at time t_4 to be positioned on the upper right propagator (index l in the figure) instead that on the lower right one.

The diagrams we have derived in this Section correspond to the so–called "left" mass–operator[2], shown in Fig. 3. Actually, in order to obtain the complete kernel of the BSE, we need to apply the same procedure to the right (or adjoint) mass–operator. The difference with Eq. (31) is that the vertex Γ^{el} appears on the left side of the diagram, with one leg at time t_1. The derivation is exactly the same as we have already done, the only change being the reflection of the "left" diagrams with respect to the central time. In this way we obtain four contributions to $\Xi^{e-p}|_L$.

An additional crucial approximation that we need to reach the final form of the Ξ^{e-p} is to neglect all internal dressings of the e–p vertexes. The physical motivation is that the DFPT approach already embodies a correlation contribution due to the DFT exchange–correlation kernel and in order to avoid double–counting errors the Γ^{el} renormalization must be neglected. Mathematically this correspond to assume in Fig. 4 and Fig. 5 $\underline{\underline{\Gamma}}^{el}\underline{\underline{D}}^{\mu} \approx \underline{\underline{D}}^{\mu}$ and to replace the interaction at time t_4 in Fig. 5 with a plain dressed vertex (■). At the same time this approximation corresponds to taking only the diagram (a) of Fig. 4.

Ultimately, if we now sum $\underline{\underline{\Xi}}^{e-p}\big|_G + \underline{\underline{\Xi}}^{e-p}\big|_L$ we finally get the final result that is shown diagrammatically in Fig. 6. We note that in order to rebuild the full $\underline{\underline{L}}$, the diagrams Fig. 6b and Fig. 6d are to be summed with the diagram Fig. 4a and its adjoint.

The final step is to move from time to frequency domain. By using the Feynman diagrams "cutting" techniques introduced in Refs. [8 and 44], it is possible to demonstrate that the Generalized BSE acquires the form

$$\underline{\underline{L}}^{opt}(\omega) = \underline{\underline{L}}^{0}(\omega)\left\{\underline{\underline{1}} + \right. \\ \left. + i\left(\underline{\underline{W}} - \underline{\underline{V}}^{H}\right) + \underline{\underline{\Xi}}^{e-p}\left[\underline{\underline{L}}^{el}\right](\omega)\right\}\underline{\underline{L}}^{opt}(\omega). \quad (45)$$

Eq. (45) is the main result of this work. The $\underline{\underline{\Xi}}^{e-p}$ kernel is a functional of the *elemental* excitonic propagator. This is a key property overlooked by previous attempts at deriving a theory of exciton–phonon coupling[41,42].

Eq. (45) demonstrates what could already be expected from the form of M^{e-p}: the *optical* exciton–phonon interaction should be written in terms of *elemental excitons*. This is not a consequence of the specific diagrammatic form of the mass operator but it is an intrinsic property of bound electron–hole pairs in a many–body treatment.

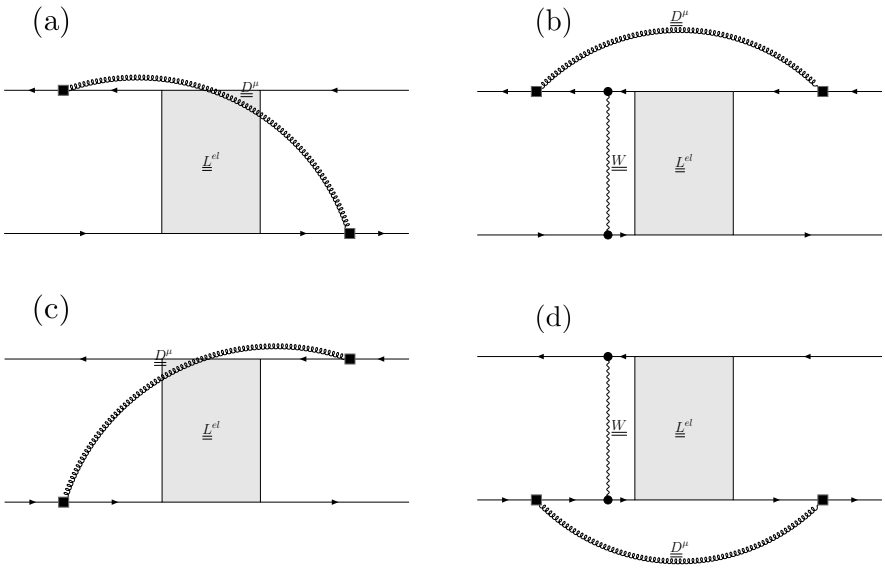


Figure 6. Final form of the exciton–phonon kernel. This is composed by four diagrams corresponding to the different possible geometries of the phonon scattering.

VI. EXCITON-PHONON IN PRACTICE

We can now rotate Eq. (45) in the *optical excitons* basis composed by the states $|\lambda\rangle^{opt}$ with energy E^{opt}_{λ} to get

$$L^{opt}_{\lambda_1\lambda_2}(\omega) = L^{opt}_{\lambda_1}(\omega)\big|_{HSEX}\left[\delta_{\lambda_1\lambda_2} + \right. \\ \left. + \Pi_{\lambda_1\lambda_3}(\omega)\, L^{opt}_{\lambda_3\lambda_2}(\omega)\right], \quad (46)$$

with

$$\Pi_{\lambda_1\lambda_2}(\omega) = \sum_{\nu\mu} \frac{\overline{\mathcal{G}^{\mu}_{\lambda_1{}^{opt}\nu^{el}}}\,\mathcal{G}^{\mu}_{\lambda_2{}^{opt}\nu^{el}}}{\omega - E^{el}_{\nu} - \Omega_{\mu} - i0^{+}} \quad (47)$$

being the exciton–phonon self–energy. In Eq. (47) we have defined the *optical–elemental* phonon–mediated scattering potential

$$\mathcal{G}^{\mu}_{\lambda^{opt}\nu^{el}} \equiv \sum_{ijl}\left(A^{ij,opt}_{\lambda}\overline{A^{il,el}_{\nu}}\,g^{\mu}_{jl} - A^{ij,opt}_{\lambda}\overline{A^{lj,el}_{\nu}}\,g^{\mu}_{il}\right). \quad (48)$$

Eq. (48), which differs from the commonly employed optical–optical version of the scattering potential, is the central result of this work for computational purposes. It shows that lattice vibrations can distinguish between total and external fields when coupling to electronic excitations.

In order to complement these equations and remarks with numerical analysis, we consider the excitonic self–energy to be diagonal. In addition, it is useful to rewrite the self–energy and the coupling matrix element exposing their momentum structure:

$$\Pi_{\alpha^{opt}q}(\omega) = \frac{1}{N_q}\sum_{\mu\beta^{el}q'} \frac{|\mathcal{G}^{\mu q'}_{\alpha^{opt}\beta^{el}q}|^2}{\omega - E_{\beta^{el}q+q'} - \Omega_{\mu q'} - \mathrm{i}\eta}, \quad (49)$$

and for the coupling we have[41,67]

$$\mathcal{G}^{\mu q'}_{\alpha^{opt}\beta^{el}q} = \sum_{cvk}\left[\sum_{v'} A^{ck,vk-q}_{\alpha^{opt}q}\overline{A^{ck,v'k-q-q'}_{\beta^{el}q+q'}}\,g^{\mu q'}_{vk,v'k-q'} - \sum_{c'} A^{ck,vk-q}_{\alpha^{opt}q}\overline{A^{c'k+q',vk-q}_{\beta^{el}q+q'}}\,g^{\mu q'}_{c'k+q',vk}\right]. \quad (50)$$

Here, the v indices correspond to valence (hole) states and the c ones to conduction (electron) states. We have calculated from first principles the exciton–phonon coupling matrix element, Eq. (50), relative to the A and B excitons of of MoS_2 and $MoSe_2$ at the Γ point ($q = 0$, $q' = 0$). We have done so using both the opt-el ($\mathcal{G}^{\mu}_{\alpha^{opt}\beta^{el}}$) and the opt-opt ($\mathcal{G}^{\mu}_{\alpha^{opt}\beta^{opt}}$) scatterings in order to compare the two approaches, showing the results in Fig. 7 for the A and B excitons for each optical phonon mode μ.

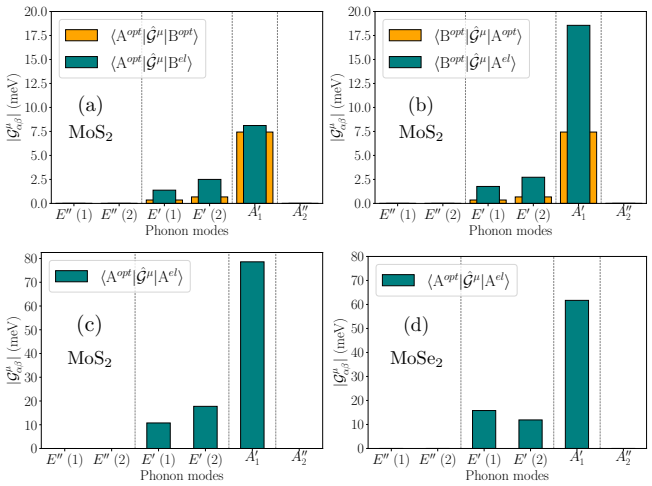


Figure 7. Strengths of the exciton–phonon matrix elements $\mathcal{G}$ between A and B excitons in $MoS_2$and $MoSe_2$with respect to the optical phonon modes at $q = 0$ (the phonon modes are labelled according to their symmetry representation). (a) and (b): comparison between opt–opt (orange) and opt–el (teal) scattering pictures in MoS_2. The couplings of exciton A^{opt} with $B^{opt/el}$ (a) and of exciton B^{opt} with $A^{opt/el}$ (b) are shown. (c) and (d): values of the A^{opt}–A^{el} couplings in the case of $MoS_2$and $MoSe_2$, respectively.

Firstly, we point out that the only active optical modes for these excitons are those with E' and A_1' symmetry.[68] Figure 7(a) and (b) display the values of $|\mathcal{G}^{\mu}_{A^{opt}B^{\eta}}|$ and $|\mathcal{G}^{\mu}_{B^{opt}A^{\eta}}|$ for MoS_2 with $\eta = opt$ (orange) and $\eta = el$ (teal). This is not a physically meaningful coupling since it is not possible for exciton A to scatter into exciton B at Γ with the aid of a single phonon due to their energy separation, yet it is useful to compare the opt–opt and opt–el cases. We see that the couplings are quite similar in terms of active phonon modes, with the opt–el matrix elements having generally a larger value. Note also that, as expected, the opt–el matrix at $q' = 0$ elements are not symmetric in the interchange of the exciton index, unlike in the opt–opt case. Figures 7(b) and 7(c) show the couplings between excitons of the same kind, in particular the A states of MoS_2 and $MoSe_2$, respectively. As the coupling with the A_1' mode is close to 100 meV in both cases, and these scatterings are permitted by energy conservation, we may expect that these matrix elements, which are absent in the opt–opt case, may play a large role in the excitonic linewidths.[69]

Indeed, from Eqs. (49) and (50) it is possible to define the (homogeneous) linewidth of exciton αq due to phonon scattering. First, we switch to the finite temperature version of the self–energy, $\Pi_{\alpha^{opt}q}(w;T)$, where T is the lattice temperature. In this case Eq. (49), which describes phonon emission at zero temperature, becomes proportional to $1 + n_B(\Omega_{\mu q'}, T)$, where n_B is the Bose–Einstein distribution for phonons. Additionally, a second term appears, this time proportional to $n_B(\Omega_{\mu q'}, T)$ and describing the phonon absorption process. Then, the linewidth can be defined as the imaginary part of the self–energy evaluated at the exciton energy, giving:

$$\gamma_{\alpha^{opt}q}(T) = \frac{2\pi}{N_q} \sum_{s\mu\beta^{el}q'} |\mathcal{G}^{\mu q'}_{\alpha^{opt}\beta^{el}q}|^2 \times \\ \times F^{(s)}_{\mu q'}(T)\delta(E_{\alpha^{opt}q} - E_{\beta^{el}q+q'} - s\Omega_{\mu q'}), \quad (51)$$

with $s = \pm$ and $F^{(s)}_{\mu q'}(T) = (1 + s)/2 + n_B(\Omega_{\mu q'}, T)$. A striking occurrence arises from this expression: the linewidth of the optical exciton α^{opt} is now determined by all the elemental excitons β^{el} it can scatter to. This means, given that elemental excitons are generally more tightly bound than optical ones, that the energy conservation condition $E_{\alpha^{opt}} = E_{\beta^{el}} + \Omega_{\mu}$ may be satisfied even for the lowest–lying optically bright exciton at zero temperature, which therefore counterintuitively acquires a finite linewidth. In order to numerically test this, we have computed the $q' = 0$ component of the linewidths, denoted as $\gamma^0_{\alpha^{opt}}$, for our excitonic states of interest.

This represents the exciton-phonon transition rates at vanishing momentum and, potentially, the most important contributions to the linewidths due to the large values of the electron-phonon coupling matrix elements for zone-center optical modes in these 2D systems.[70–72] This quantity is sufficient to assess if the A (and B) excitons have a finite linewidth or not. The results for $\gamma^0_{\alpha^{opt}}$ are plotted in Fig. 8 as a function of temperature for the A and B excitons of MoS_2 ((a) and (b), respectively) and for the A exciton of $MoSe_2$ (case (c)). The red diamonds represent the opt–el case, while the blue circles refer to the opt–opt scatterings (the lightly shaded region corresponds to the contribution of the phonon emission term; the barely visible darkly shaded region is due to the phonon absorption term). We see that in the opt–opt case the $q = 0$ transition rates are always negligibly small, as expected. However, in the case of the opt–el scattering, the same quantity for the A excitons *starts with a finite value* around 4 meV, even though these states are the lowest–bound optical excitons in the two systems considered. The B exciton has a much larger value as well.

We note that the opt–el scattering also affects the energy position of the phonon–assisted satellite replicas in absorption or emission spectra[41,44,67] (in addition to their linewidths), since the poles of the self–energy in Eq. (49) are different than in the opt–opt case — the difference being $E_{\beta^{opt}} - E_{\beta^{el}}$. For example, the optical absorption satellites relative to exciton α^{opt} (with $q = 0$) will appear at energy $E_{\alpha^{opt}} + E_{\beta^{el}q'} - s\Omega_{\mu q'}$ instead of $E_{\alpha^{opt}} + E_{\beta^{opt}q'} - s\Omega_{\mu q'}$.

VII. DISCUSSION

In this work we stressed and formally demonstrated the importance of considering "excitons" as a product of the measurement process, i.e., as the response of the electronic system to a specific external experimental field,

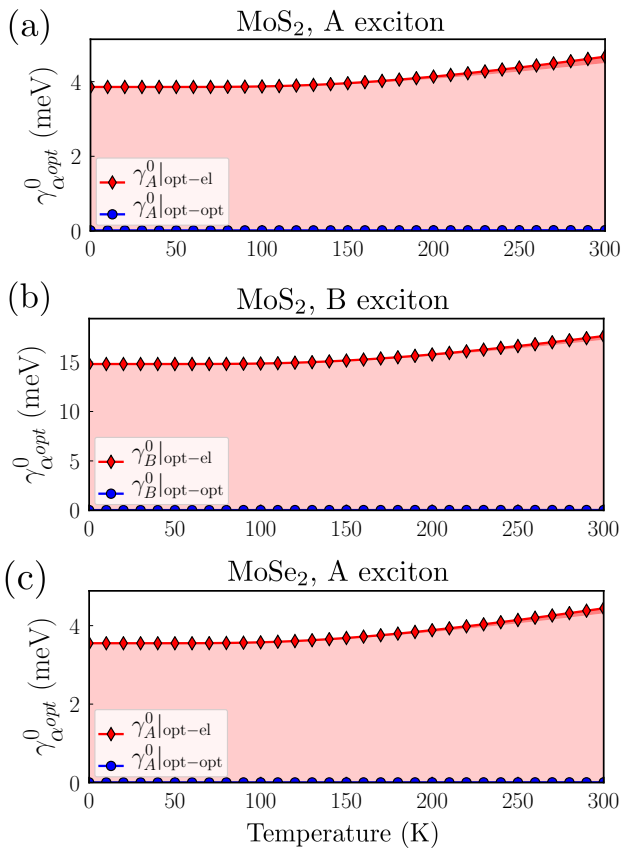


Figure 8. Sum of the exciton-phonon transition rates at vanishing momentum $\gamma^0_{\alpha^{opt}}$ as a function of temperature (see text) for select excitonic states in the optical–elemental scattering picture (red line and diamonds) and in the optical–optical scattering picture (blue line and circles). (a) MoS_2, A exciton. (b) MoS_2, B exciton. (c) A $MoSe_2$, A exciton. The lightly shaded (darkly shaded, barely visibile on the top) red area represents the phonon emission (phonon absorption) contribution to $\gamma^0_{\alpha^{opt}}$.

instead of thinking about them as real particles. In the case of the exciton–phonon problem, this leads to the optical–elemental scattering picture rather than the optical–optical picture. Here we discuss several possible directions of future investigations. As for how to compare theory and experiment, at the end of this Section we outline the main underlying challenges.

Excitons as real particles. It may be possible, under specific experimental conditions (such as low excitation density, equilibrium–like steady state of exciton generation and recombination), to reduce the physics of a photo–excited system to simple objects. However it does not seem possible, at the same time, to write a theory of exciton dynamics in terms of excitonic boson states. In general, the difference between the optical–elemental and optical–optical pictures may be small in materials where $|V^H| << |W^{SEX}|$, while it may be sizable in systems where this does not hold. According to our calculations, the ratios of $|V^H|$ to $|W^{SEX}|$ for the excitons analysed in this paper are: 2.4% (A exciton, monolayer MoS_2), 4.0% (B exciton, monolayer MoS_2), and 2.8% (A exciton, monolayer $MoSe_2$). This is sufficient to cause level crossings between bright and dark states and sensibly alter the exciton dispersion landscape at low finite momenta (see Fig. 2).

Photo–luminescence. In general it is well known that the frequency of the emitted light may be different from the one corresponding to the peak absorption (one striking case is the upconversion effect[73]). Since photo–luminescence is a recombination process involving real excitations of the system, it is possible that this is purely governed by elemental states, leading to different energies and linewidths. In other words, our theory suggests that the emission linewidths and their time–domain counterparts, "exciton" relaxation times, should be different from absorption linewidths and *decoherence* times (only the latter linewidths having a finite value at $T = 0$).

Ultra–fast physics and excitonic dynamics. What dictates the dynamics following a photo–excitation? Our hypothesis is that the initial excitation does not project the system in a specific and well–defined ("optical") excited state but, rather, to a packet of ("elemental") excited states, e.g., the energetically accessible section of the distributions in Fig. 2(c–d). This means that the dynamics that follows depends, unavoidably, from the excitation itself. In addition, and more importantly, the physics of this evolution cannot be described entirely in terms of *optical excitons*.

Comparison between theory and experiment. Unfortunately, the comparison of ab initio, parameter–less theory and experiment is very difficult in these kinds of systems. On the theory side, TMD exciton linewidths and phonon–assisted optical spectra carry unknown uncertainties because they depend on the relative positions of the many valleys appearing in the exciton dispersions of these materials. These valleys in turn depend enormously on tiny details of the underlying electronic band structures, and are affected both by pseudopotential details (DFT level) and quality of the k–dependent quasiparticle approximation employed (many–body level). The severity of these problems increases with the atomic number of the elements forming the TMD compound (particularly if Se, Te, or W are present). From the experimental point of view, it is very difficult to disentangle the phonon contribution to the exciton linewidths from other effects. In particular, beyond the phonon contributions, linewidths are also compounded by the probability of radiative recombination, substrate and encapsulation dependence and inhomogeneities due to disorder, defects and strain. In order to unambiguously check our predictions, we would need an experimental setup able to measure either exciton absorption linewidths (in the frequency domain) or exciton decoherence times (in the time domain) on a very clean sample and with an accuracy around 1 meV / 5 ps while reliably discarding the radiative recombination contributions. In recent years, attempts have been made theoretically and experimen-

tally to quantify the latter contribution[12,64,74–78]. In addition, multidimensional optical spectroscopy (MDOS) experiments[79,80] have allowed for the extraction of the homogeneous part of the linewidths from the inhomogeneous one, leading in many cases to a reduction of about one order of magnitude in observed linewdiths between MDOS and photoluminescence experiments[11,61,81,82]. In general, MDOS experiments measure values below 10 meV for the A exciton linewidths at low temperatures. Using these techniques, experimentalists are now able to probe the roles of electron–hole exchange and phonon interactions in the exciton dynamics in real time[61,83]. Despite all the current advances, unresolved differing theoretical and experimental estimates for the A exciton linewidths of MoS_2 and $MoSe_2$ are still present in the cited literature — with no estimates to our knowledge for the B exciton of MoS_2. For example, in the case of the A exciton of $MoSe_2$, Ref. [82] finds a broadening of less than 1 meV — consistent with what the optical–optical scattering would predict, while Ref. [81] finds a homogeneous value of around 5 meV for both MoS_2 and $MoSe_2$, proposing intrinsic electron–phonon interactions as the limiting factor: the latter interpretation is quite consistent with our findings. Both are MDOS experiments.

VIII. CONCLUSION

We have developed a theory of exciton–phonon coupling starting from the many–body interacting electronic Hamiltonian, in the presence of both an external electromagnetic field and electron–phonon interaction. In deriving the theory, we have used only those approximations and assumptions already underlying first–principles treatments of optical excitations and lattice vibrations, without adding additional ones, such as bosonized excitons, which are often employed in the literature. Our main finding is that exciton–phonon interaction fundamentally distinguishes between the responses of the electron system to the external and total fields, coupling the excitations that describe the first (optical, reducible) and the second (elemental, irreducible). Using the examples of monolayer MoS_2 and $MoSe_2$ — two paradigmatic materials belonging to the highly interesting class of layered semiconductors — we have also shown how the exciton–phonon matrix elements and linewidths can be qualitatively different with respect to the case when only a single exciton "type" is considered. Therefore, we believe that our work may be valuable for the interpretation and calculation of various exciton–phonon related phenomena, namely exciton linewidths and broadening, phonon–assisted absorption, emission and reflectivity measurements in the presence of excitons, and the complex nonequilibrium problem of exciton dynamics. On the computational side, a full implementation of exciton–phonon interactions is ongoing in the Yambo code[84,85], with the aim of computing accurate linewidths and luminescence spectra including finite–momentum integrals in the Brillouin zone. On the theoretical side, two very promising avenues of research are represented by the derivation of a consistent theory for incoherent exciton relaxation (including the coherent–to–incoherent crossover) and the investigation of the dynamical effects of electronic screening on the electron–hole–phonon composite excitation.

IX. ACKNOWLEDGEMENTS

We gratefully thank C. Attaccalite, D. Sangalli and M. Zanfrognini for precious insight on the numerical simulations and testing of the finite–q BSE and of the electron–phonon and exciton–phonon couplings. We are also indebted to M. Palummo for sharing input files for the GW–BSE calculations of $MoSe_2$based on Ref. [86] and for discussions about pseudopotentials.

We acknowledge the funding received from the European Union projects: MaX *Materials design at the eXascale* H2020-EINFRA-2015-1, Grant agreement n. 676598, and H2020-INFRAEDI-2018-2020/H2020-INFRAEDI-2018-1, Grant agreement n. 824143; *Nanoscience Foundries and Fine Analysis - Europe* H2020-INFRAIA-2014-2015, Grant agreement n. 654360.

Appendix A: External and induced fields

In Eq. (1) we have used as external perturbation the *total* macroscopic potential U^{ext} which includes the induced potential. This is a mathematical short way to introduce *optical excitons* directly from the response function defined in Eq. (3). In reality the Hamiltonian contains just the external, bare potential, V^{ext} whose dressing by the local, induced potential should appear dynamically[87–90].

Mathematically this corresponds to define the total Hartree potential as

$$V^{H,TOT}(\mathbf{r},t) = \int \mathrm{d}\mathbf{r}' \rho(\mathbf{r}',t)\, v(\mathbf{r},\mathbf{r}'), \qquad \text{(A1)}$$

so that $U^{ext}(\mathbf{r},t) = V^{ext}(\mathbf{r},t) + \int d\mathbf{r} V^{H,TOT}(\mathbf{r},t)$. It follows that Eq. (2) contains just the microscopic part of the Hartree potential

$$V^{H}(\mathbf{r},t) = V^{H,TOT}(\mathbf{r},t) - \int d\mathbf{r} V^{H,TOT}(\mathbf{r},t). \qquad \text{(A2)}$$

The exciton–phonon derivation is totally independent on the definition of the external potential. It is in fact possible, without changing anything in the theory, to take as U^{ext} just the external, experimental field V^{ext}, leaving the macroscoping average of $V^{H,TOT}$ together with the rest of the electron–electron interaction terms in Eq. (1). In this case the present theory may be said to describe *plasmon*–phonon scattering.

Appendix B: Mathematical conventions

In considering operations among matrices, vectors and tensors we will use the following convention

$$\left[\underline{V}\,\underline{\underline{M}}\right]_{\substack{ij\\kl}} = V_{im} M_{\substack{mj\\kl}}, \tag{B1a}$$

$$\left[\underline{\underline{M}}\,\underline{V}\right]_{\substack{ij\\kl}} = M_{\substack{im\\kl}} V_{mj}, \tag{B1b}$$

$$\left[\underline{\underline{M}}\,\underline{\underline{O}}\right]_{\substack{ij\\kl}} = M_{\substack{ij\\pq}} O_{\substack{pq\\kl}}. \tag{B1c}$$

In Eq. (B1) we use the Einstein convention that all repeated indices are summed. Notice also that the generalised single–particle indices may be transformed in Bloch–state indices by explicitly by replacing i and j with band (n, m) and crystal momentum (k, k') indices:

$$i \to nk, \tag{B2a}$$

$$j \to mk', \tag{B2b}$$

$$\lambda \to \alpha q, \tag{B2c}$$

where the last index λ refers to the excitonic basis, with α indicating the exciton "branch" and $q = k - k'$ its momentum. We will use the generalised indices as much as possible in order to lighten the equations, switching to the other ones when needed.

Appendix C: The Bethe–Salpeter Hamiltonian

The *optical*–BSE Hamiltonian emerges when the retarded time ordering in t_1 and t_2 is considered ($t_1 > t_2$) and the equations are solved in frequency space by by applying the Laplace transform to the time difference $t_1 - t_2$.

The noninteracting part of the BSE, $\underline{\underline{L}}^0(t_1, t_2) \equiv \underline{G}(t_1, t_2)\,\underline{\delta}\,\underline{G}(t_2, t_1)$, can be Laplace transformed and results in

$$L^0_{\substack{ij\\kl}}(\omega) = i\delta_{ik}\delta_{jl}\left(f_j - f_i\right)\left[\omega + i0^+ - (\epsilon_i - \epsilon_j)\right]^{-1}, \tag{C1}$$

where f_i represents a single–particle occupation factor. Then, Eq. (20) can be rewritten as

$$\underline{\underline{L}}^{opt}(\omega) = \left[\left(\underline{\underline{L}}^0(\omega)\right)^{-1} - i\left(\underline{\underline{W}} - \underline{\underline{V}}^H\right)\right]^{-1}. \tag{C2}$$

Eq. (C2) is an exact way to rewrite the BSE in the case of interacting neutral excitations (optical excitons, our focus here, or plasmons). At this point the introduction of an effective Hamiltonian can be done by observing that Eq. (C2) can be rewritten using Eq. (C1) as

$$\left[\underline{\underline{L}}^{opt}(\omega)\right]^{-1}_{\substack{ij\\kl}} = -i\left(f_j - f_i\right)^{-1}\left(\delta_{ik}\delta_{jl}\left(\omega + i0^+\right) - \mathcal{H}^{opt}_{\substack{ij\\kl}}\right), \tag{C3}$$

with

$$\mathcal{H}^{opt}_{\substack{ij\\kl}} = \delta_{ik}\delta_{jl}\left(\epsilon_i - \epsilon_j\right) - \left(f_j - f_i\right)\left(W_{\substack{ij\\kl}} - K^{opt}_{\substack{ij\\kl}}\right). \tag{C4}$$

Appendix D: Computational details

In this Appendix we provide extensive computational details regarding our many–body, first–principles simulations[1,5] of monolayers MoS_2 and $MoSe_2$. The density functional theory[91] (DFT) simulations of the electronic ground state and the Kohn–Sham eigenvalues were done with Quantum ESPRESSO[92,93] (QE). This code was also used for the density functional perturbation theory[94,95] (DFPT) calculation of the phonon frequencies and electron–phonon matrix elements. The many–body simulations, using DFT as a starting point, were performed with the Yambo code[96]. They include the use of the G_0W_0 approximation[97,98] for the quasiparticle corrections to the Kohn–Sham eiganvalues, as well as the state–of–the–art BSE[99] simulations of excitonic properties.

DFT and DFPT. We used norm–conserving, fully relativistic pseudopotentials[100] (GGA–PBE type) and included spin–orbit interaction at all stages of the calculations, working with spinorial wave functions[86]. Our 2D hexagonal systems have lattice parameter $a = 5.90$ (MoS_2) and $a = 6.15$ ($MoSe_2$) bohrs, with about 40 bohrs of vacuum separating repeated copies of the simulation supercells in the c direction. A 2D Coulomb cutoff technique was used both at the DFT/DFPT level[70], in order to correctly compute phonon–related quantities at vanishing momentum, and at the many–body stage. The kinetic energy cutoff on the wave functions were 140 Ry (MoS_2) and 90 Ry ($MoSe_2$), and the ground–state charge density was converged in both cases with a $12 \times 12 \times 1$ grid of k–points in momentum space. Unoccupied Kohn–Sham bands, phonon frequencies, phonon eigenvectors and the variations in the self–consistent DFT potential were then computed on this charge density. We checked that both the Kohn–Sham band structures and the phonon dispersion curves were in agreement with previous calculations. Electron–phonon matrix elements were computed on a $39 \times 39 \times 1$ k–grid to match the one used for excitons.

Many–body. The quasiparticle corrections for MoS_2were simulated using a simple scissor operator enforcing a rigid shift of the bands by 1 eV, which was enough for our purposes. For $MoSe_2$we used instead the quasiparticle corrections previously calculated in Ref. [86] at the G_0W_0 level, where the relevant details may be found. We computed the BSE both with (reducible, optical) and without (irreducible, elemental) the exchange contribution to the excitonic kernel, all in the Tamm–Dancoff approximation[101] (i.e., the kernel includes only resonant or antiresonant electron–hole transitions; this common approximation usually works well for gapped semiconductors and is a requirement for the exciton–phonon treatment). We used a dense grid of $39 \times 39 \times 1$ k–points for both systems. The RPA static screening was computed with an energy cutoff of 8 Ry, using 100 empty states in both cases. The energy cutoff for the exchange part of the kernel was set to 60 Ry (MoS_2) and 40 Ry

($MoSe_2$) when included in the calculations. The cutoff on the RPA screened interaction was 8 Ry for both systems. The electronic transitions included in the BSE kernel were comprised in both cases of the two top valence and the two bottom conduction states, properly including the spin–orbit splitting at the K and K' points in the BZ. We checked that our calculated optical absorption spectra are in agreement with existing calculations[86]. For the finite–q BSE calculations, Fig. 2e–f, we also checked that our results are in agreement with existing literature.[58]

Exciton–phonon. The phonon frequencies, eigenvectors and electron–phonon matrix elements were read from the DFPT–QE calculations and converted to the Yambo format. Then, these quantities along with the exciton energies and k–space exciton wave functions from the BSE–Yambo calculations were combined using the Yambopy package[102] in order to compute the exciton–phonon coupling matrix elements, Eq. (50), at $q = 0$. We note that the capability to compute various exciton–phonon related quantities, including integrations over q, is currently being developed in the Yambo code. Concerning the $q' = 0$ component of the linewidth, $\gamma^0_{\alpha^{opt}}$ in Eq. (51), a numerical broadening factor of 1 meV was used for the delta function. Sixteen excitonic states were included in the sum: this is enough to converge the value of $\gamma^0_{\alpha^{opt}}$ within 0.01 meV for the excitonic states considered (note that many more states may be necessary to converge the real part of the self–energy[42]). Each plot in Figs. 7 and 8 is summed over the two components of the doubly degenerate A and B states.

* fulvio.paleari@nano.cnr.it

1 G. Onida, L. Reining, and A. Rubio, Rev. Mod. Phys. **74**, 601 (2002).

2 G. Strinati, La Rivista del Nuovo Cimento (1978-1999) **11**, 1 (1988), 10.1007/BF02725962.

3 M. G. C. Attaccalite and A. Marini, Phys. Rev. B **84**, 245110 (2011).

4 F. Bechstedt, *Many-Body Approach to Electronic Excitations* (Springer, 2015).

5 R. M. Martin, L. Reining, and D. M. Ceperley, *Interacting electrons – Theory and Computational Approaches* (Cambridge University Press, 2016).

6 In many–body theory they correspond to the poles of the so–called reducible response function[2]. They are also called "singlet" or "transverse" excitons[88,103] depending on the context.

7 K. S. Thygesen, 2D Materials **4**, 022004 (2017).

8 A. Marini and R. Del Sole, Phys. Rev. Lett. **91**, 176402 (2003).

9 M. Grüning, A. Marini, and X. Gonze, Nano Letters **9**, 2820 (2009), pMID: 19637906, http://pubs.acs.org/doi/pdf/10.1021/nl803717g.

10 A pseudo–Hermitian matrix admits different left ($\langle\lambda_L|$) and right ($|\lambda_R\rangle$) eigenvectors. Both with the same, real frequency. It is, therefore, impossible to introduce an *excitonic* creation operator $\hat{B}^\dagger_\lambda$ to write $|\lambda_R\rangle = \hat{B}^\dagger_\lambda|0\rangle$ as this would imply $\langle\lambda_R|$ to be an eigenstate but different from $\langle\lambda_L|$.

11 G. Moody, C. Kavir Dass, K. Hao, C.-H. Chen, L.-J. Li, A. Singh, K. Tran, G. Clark, X. Xu, G. Berghäuser, E. Malic, A. Knorr, and X. Li, Nature Communications **6**, 8315 (2015).

12 M. Selig, G. Berghäuser, A. Raja, P. Nagler, C. Schüller, T. F. Heinz, T. Korn, A. Chernikov, E. Malic, and A. Knorr, Nat Commun **7**, 026803 (2016).

13 D. Christiansen, M. Selig, E. Malic, R. Ernstorfer, and A. Knorr, Phys. Rev. B **100**, 205401 (2019).

14 C. Trovatello, F. Katsch, N. J. Borys, M. Selig, K. Yao, R. Borrego-Varillas, F. Scotognella, I. Kriegel, A. Yan, A. Zettl, P. J. Schuck, A. Knorr, G. Cerullo, and S. D. Conte, Nat Commun **11**, 216805 (2020).

15 S. Dong, M. Puppin, T. Pincelli, S. Beaulieu, D. Christiansen, H. Hübener, C. W. Nicholson, R. P. Xian, M. Dendzik, Y. Deng, Y. W. Windsor, M. Selig, E. Malic, A. Rubio, A. Knorr, M. Wolf, L. Rettig, and R. Ernstorfer, Natural Sciences **1**, 205401 (2021).

16 J. Madéo, M. K. L. Man, C. Sahoo, M. Campbell, V. Pareek, E. L. Wong, A. Al-Mahboob, N. S. Chan, A. Karmakar, B. M. K. Mariserla, X. Li, T. F. Heinz, T. Cao, and K. M. Dani, Science **370**, 1199 (2020).

17 M. Dendzik, R. P. Xian, E. Perfetto, D. Sangalli, D. Kutnyakhov, S. Dong, S. Beaulieu, T. Pincelli, F. Pressacco, D. Curcio, S. Y. Agustsson, M. Heber, J. Hauer, W. Wurth, G. Brenner, Y. Acremann, P. Hofmann, M. Wolf, A. Marini, G. Stefanucci, L. Rettig, and R. Ernstorfer, Phys. Rev. Lett. **125**, 096401 (2020).

18 S. W. Koch, M. Kira, G. Khitrova, and H. M. Gibbs, Nature Materials **5**, 523 (2006).

19 F. Katsch, M. Selig, A. Carmele, and A. Knorr, Phys. Status Solidi B **255**, 1800185 (2018).

20 A. Thränhardt, S. Kuckenberg, A. Knorr, T. Meier, and S. W. Koch, Phys. Rev. B **62**, 2706 (2000).

21 M. Kira and S. Koch, Progress in Quantum Electronics **30**, 155 (2006).

22 B. Miller, J. Lindlau, M. Bommert, A. Neumann, H. Yamaguchi, A. Holleitner, A. Högele, and U. Wurstbauer, Nature Communications **10**, 807 (2019).

23 H. Tanimura, K. Tanimura, and P. H. M. van Loosdrecht, Phys. Rev. B **100**, 115204 (2019).

24 E. Perfetto, D. Sangalli, M. Palummo, A. Marini, and G. Stefanucci, J. Chem. Theory Comput. **15**, 4526 (2019).

25 T. Östreich and K. Schönhammer, Zeitschrift für Physik B Condensed Matter **91**, 189 (1993).

26 A. Rustagi and A. F. Kemper, Phys. Rev. B **97**, 235310 (2018).

27 A. F. Kemper and A. Rustagi, "Observing coherences with time-resolved photoemission," (2020), arXiv:2005.08978 [cond-mat.mes-hall].

28 H. J. W. Haug and A.-P. Jauho, *Quantum Kinetics in Transport and Optics of Semiconductors* (Springer, 2008).

29 S. Ovesen, S. Brem, C. Linderälv, M. Kuisma, T. Korn, P. Erhart, M. Selig, and E. Malic, Communications Physics **2**, 23 (2019).

30 F. Katsch, M. Selig, and A. Knorr, Phys. Rev. Lett. **124**, 257402 (2020).

31 G. Mahan, *Many-Particle Physics* (Plenum, 1990).

[32] G. H. Wannier, Phys. Rev. **52**, 191 (1937).
[33] R. J. Elliott, Phys. Rev. **108**, 1384 (1957).
[34] V. Smejkal, F. Libisch, A. Molina-Sanchez, C. Trovatello, L. Wirtz, and A. Marini, ACS Nano **15**, 1179 (2021).
[35] Combescot, M. and Betbeder-Matibet, O., Europhys. Lett. **58**, 87 (2002).
[36] M. Combescot and O. Betbeder-Matibet, Phys. Rev. Lett. **93**, 016403 (2004).
[37] M. Combescot, O. Betbeder-Matibet, and R. Combescot, Phys. Rev. B **75**, 174305 (2007).
[38] Y. Toyozawa, Progress of Theoretical Physics **20**, 53 (1958), https://academic.oup.com/ptp/article-pdf/20/1/53/5457877/20-1-53.pdf.
[39] B. Segall and G. D. Mahan, Phys. Rev. **171**, 935 (1968).
[40] Y. Toyozawa, *Optical Processes in Solids* (Cambridge University Press, 2003).
[41] H.-Y. Chen, D. Sangalli, and M. Bernardi, Phys. Rev. Lett. **125**, 107401 (2020).
[42] G. Antonius and S. G. Louie, Phys. Rev. B **105**, 085111 (2022).
[43] P. Cudazzo and L. Reining, Phys. Rev. Research **2**, 012032(R) (2020).
[44] P. Cudazzo, Phys. Rev. B **102**, 045136 (2020).
[45] E. Baldini, A. Dominguez, T. Palmieri, O. Cannelli, A. Rubio, P. Ruello, and M. Chergui, Science Advances **5** (2019), 10.1126/sciadv.aax2937, https://advances.sciencemag.org/content/5/11/eaax2937.full.pdf.
[46] S. Rudin, T. L. Reinecke, and B. Segall, Phys. Rev. B **42**, 11218 (1990).
[47] V. Perebeinos, J. Tersoff, and P. Avouris, Phys. Rev. Lett. **94**, 027402 (2005).
[48] E. Cannuccia, B. Monserrat, and C. Attaccalite, Phys. Rev. B **99**, 081109(R) (2019).
[49] F. Paleari, H. P. C. Miranda, A. Molina-Sánchez, and L. Wirtz, Phys. Rev. Lett. **122**, 187401 (2019).
[50] S. Reichardt and L. Wirtz, Science Advances **6** (2020), 10.1126/sciadv.abb5915, https://advances.sciencemag.org/content/6/32/eabb5915.full.pdf.
[51] In this paper we use the term *elemental excitons* for simplicity. These states correspond, in many–body theory, to the poles of the *irreducible* response function and hence may also be called irreducible excitons. They also correspond to the "triplet"[86] or "Ising" excitons[61] in spin–polarised systems.
[52] E. Perfetto, D. Sangalli, A. Marini, and G. Stefanucci, Phys. Rev. B **92**, 205304 (2015).
[53] C. Attaccalite, M. Grüning, and A. Marini, Phys. Rev. B **84**, 245110 (2011).
[54] G. Pal, Y. Pavlyukh, H. C. Schneider, and W. H?bner, The European Physical Journal B - Condensed Matter and Complex Systems **70**, 483 (2009), 10.1140/epjb/e2009-00253-9.
[55] A. Marini, S. Poncé, and X. Gonze, Phys. Rev. B **91**, 224310 (2015).
[56] G. Stefanucci and R. van Leeuwen, *Nonequilibrium Many-Body Theory of Quantum Systems* (Cambridge University Press, 2013).
[57] R. van Leeuwen, Phys. Rev. B **69**, 115110 (2004).
[58] T. Deilmann and K. S. Thygesen, Phys. Rev. B **96**, 201113(R) (2017).
[59] C. Robert, B. Han, P. Kapuscinski, A. Delhomme, C. Faugeras, T. Amand, M. R. Molas, M. Bartos, K. Watanabe, T. Taniguchi, B. Urbaszek, M. Potemski, and X. Marie, Nature Communications **11**, 4037 (2020).
[60] A. Arora, K. Nogajewski, M. Molas, M. Koperski, and M. Potemski, Nanoscale **7**, 20769 (2015).
[61] L. Guo, M. Wu, T. Cao, D. M. Monahan, Y.-H. Lee, S. G. Louie, and G. R. Fleming, Nature Physics **15**, 228 (2019).
[62] D. Y. Qiu, T. Cao, and S. G. Louie, Phys. Rev. Lett. **115**, 176801 (2015).
[63] M. Selig, G. Berghäuser, A. Raja, P. Nagler, C. Schüller, T. F. Heinz, T. Korn, A. Chernikov, E. Malic, and A. Knorr, in *Ultrafast Phenomena and Nanophotonics XXI*, Vol. 10102, edited by M. Betz and A. Y. Elezzabi, International Society for Optics and Photonics (SPIE, 2017) pp. 160 – 168.
[64] J. C. G. Henriques, N. A. Mortensen, and N. M. R. Peres, Phys. Rev. B **103**, 235402 (2021).
[65] F. Giustino, Rev. Mod. Phys. **89**, 015003 (2017).
[66] Indeed, even by performing the two neglected functional derivatives it is possible to show that they lead to the renormalization of the electron–phonon and electron–electron interaction. In diagrammatic language this means that they produce diagrammatic geometries that can be reduced with respect to a W and/or D internal propagator.
[67] F. Paleari, *First-principles approaches to the description of indirect absorption and luminescence spectroscopy: exciton-phonon coupling in hexagonal boron nitride*, Ph.D. thesis, Physics and Materials Science Research Unit, University of Luxembourg (2019).
[68] A. Molina-Sánchez, K. Hummer, and L. Wirtz, Surface Science Reports **70**, 554 (2015).
[69] Note that the A_2'' mode, i.e., the longitudinal optical mode, is identically zero in our $q = 0$ calculation because the long–range Coulomb interaction was not added to the electron–phonon matrix elements[70]. This mode is therefore not considered in the evaluation of exciton–phonon transition rates.
[70] T. Sohier, M. Calandra, and F. Mauri, Phys. Rev. B **94**, 085415 (2016).
[71] W. H. Sio and F. Giustino, "Unified ab initio description of fröhlich electron-phonon interactions in two-dimensional and three-dimensional materials," (2022), arXiv:2203.00568.
[72] Z. Jin, X. Li, J. T. Mullen, and K. W. Kim, Phys. Rev. B **90**, 045422 (2014).
[73] B. Han, C. Robert, E. Courtade, M. Manca, S. Shree, T. Amand, P. Renucci, T. Taniguchi, K. Watanabe, X. Marie, L. E. Golub, M. M. Glazov, and B. Urbaszek, Phys. Rev. X **8**, 031073 (2018).
[74] M. Palummo, M. Bernardi, and J. C. Grossman, Nano Letters **15**, 2794 (2015), pMID: 25798735, http://dx.doi.org/10.1021/nl503799t.
[75] H. Wang, C. Zhang, W. Chan, C. Manolatou, S. Tiwari, and F. Rana, Phys. Rev. B **93**, 045407 (2016).
[76] S. Brem, M. Selig, G. Berghaeuser, and E. Malic, Scientific Reports **8**, 8238 (2018).
[77] S. Roux, C. Arnold, F. Paleari, L. Sponza, E. Janzen, J. H. Edgar, B. Toury, C. Journet, V. Garnier, P. Steyer, T. Taniguchi, K. Watanabe, F. Ducastelle, A. Loiseau, and J. Barjon, Phys. Rev. B **104**, L161203 (2021).
[78] G. Cassabois, G. Fugallo, C. Elias, P. Valvin, A. Rousseau, B. Gil, A. Summerfield, C. J. Mellor, T. S. Cheng, L. Eaves, C. T. Foxon, P. H. Beton, M. Lazzeri, A. Segura, and S. V. Novikov, Phys. Rev. X **12**, 011057 (2022).
[79] S. T. Cundiff and S. Mukamel, Physics Today **66**, 44

(2013), https://doi.org/10.1063/PT.3.2047.
[80] G. Moody and S. T. Cundiff, Advances in Physics: X **2**, 641 (2017), pMID: 28894306, https://doi.org/10.1080/23746149.2017.1346482.
[81] P. Dey, J. Paul, Z. Wang, C. E. Stevens, C. Liu, A. H. Romero, J. Shan, D. J. Hilton, and D. Karaiskaj, Phys. Rev. Lett. **116**, 127402 (2016).
[82] E. W. Martin, J. Horng, H. G. Ruth, E. Paik, M.-H. Wentzel, H. Deng, and S. T. Cundiff, Phys. Rev. Applied **14**, 021002(R) (2020).
[83] D. Li, C. Trovatello, S. Dal Conte, M. Nuß, G. Soavi, G. Wang, A. C. Ferrari, G. Cerullo, and T. Brixner, Nature Communications **12**, 954 (2021).
[84] D. Sangalli, A. Ferretti, H. Miranda, C. Attaccalite, I. Marri, E. Cannuccia, P. M. Melo, M. Marsili, F. Paleari, A. Marrazzo, G. Prandini, P. Bonfà, M. O. Atambo, F. Affinito, M. Palummo, A. M. Sanchez, C. Hogan, M. Grüning, D. Varsano, and A. Marini, Journal of Physics: Condensed Matter **31**, 325902 (2019).
[85] M. G. D. V. Andrea Marini, Conor Hogan, Computer Physics Communications **180**, 1392 (2009).
[86] M. Marsili, A. Molina-Sánchez, M. Palummo, D. Sangalli, and A. Marini, Phys. Rev. B **103**, 155152 (2021).
[87] A. Yamada and K. Yabana, Phys. Rev. B **99**, 245103 (2019).
[88] V. Ambegaokar and W. Kohn, Phys. Rev. **117**, 423 (1960).
[89] K. Ehara and K. Cho, Solid State Communications **44**, 453 (1982).
[90] K. Cho, J. Phys. Soc. Jpn. **68**, 683 (1999).
[91] W. Kohn and L. J. Sham, Phys. Rev. **140**, A1133 (1965).
[92] P. Giannozzi, S. Baroni, N. Bonini, M. Calandra, R. Car, C. Cavazzoni, C. Davide, G. L. Chiarotti, M. Cococcioni, I. Dabo, A. D. Corso, S. de Gironcoli, S. Fabris, G. Fratesi, R. Gebauer, U. Gerstmann, C. Gougoussis, A. Kokalj, M. Lazzeri, L. Martin-Samos, N. Marzari, F. Mauri, R. Mazzarello, S. Paolini, A. Pasquarello, L. Paulatto, C. Sbraccia, S. Scandolo, G. Sclauzero, A. P. Seitsonen, A. Smogunov, P. Umari, and R. M. Wentzcovitch, Journal of Physics: Condensed Matter **21**, 395502 (2009).
[93] P. Giannozzi, O. Andreussi, T. Brumme, O. Bunau, M. B. Nardelli, M. Calandra, R. Car, C. Cavazzoni, D. Ceresoli, M. Cococcioni, N. Colonna, I. Carnimeo, A. D. Corso, S. de Gironcoli, P. Delugas, R. A. DiStasio, A. Ferretti, A. Floris, G. Fratesi, G. Fugallo, R. Gebauer, U. Gerstmann, F. Giustino, T. Gorni, J. Jia, M. Kawamura, H.-Y. Ko, A. Kokalj, E. Küçükbenli, M. Lazzeri, M. Marsili, N. Marzari, F. Mauri, N. L. Nguyen, H.-V. Nguyen, A. O. de-la Roza, L. Paulatto, S. Poncé, D. Rocca, R. Sabatini, B. Santra, M. Schlipf, A. P. Seitsonen, A. Smogunov, I. Timrov, T. Thonhauser, P. Umari, N. Vast, X. Wu, and S. Baroni, Journal of Physics: Condensed Matter **29**, 465901 (2017).
[94] S. Baroni, S. de Gironcoli, A. Dal Corso, and P. Giannozzi, Rev. Mod. Phys. **73**, 515 (2001).
[95] X. Gonze and C. Lee, Phys. Rev. B **55**, 10355 (1997).
[96] D. Sangalli, A. Ferretti, H. Miranda, C. Attaccalite, I. Marri, E. Cannuccia, P. Melo, M. Marsili, F. Paleari, A. Marrazzo, G. Prandini, P. Bonfà, M. O. Atambo, F. Affinito, M. Palummo, A. Molina-Sánchez, C. Hogan, M. Grüning, D. Varsano, and A. Marini, J. Phys. Condens. Matter **31**, 325902 (2019).
[97] L. Hedin, J. Phys. Condens. Matter **11**, R489 (1999).
[98] M. S. Hybertsen and S. G. Louie, Phys. Rev. B **34**, 5390 (1986).
[99] S. Albrecht, L. Reining, R. Del Sole, and G. Onida, Phys. Rev. Lett. **80**, 4510 (1998).
[100] D. R. Hamann, Phys. Rev. B **88**, 085117 (2013).
[101] S. M. Dancoff, Phys. Rev. **78**, 382 (1950).
[102] Yambopy is a python pre–postprocessing tool for QE and Yambo. It is currently under development, but a public version of the code is already available on the Yambo website.
[103] R. Del Sole and E. Fiorino, Phys. Rev. B **29**, 4631 (1984).